



HAL
open science

Very high cycle fatigue durability of an additively manufactured single-crystal Ni-based superalloy

Luciana Maria Bortoluci Ormastroni, Inmaculada Lopez-Galilea, Julian Pistor, Benjamin Rutttert, Carolin Körner, Werner Theisen, Patrick Villechaise, Fernando Pedraza, Jonathan Cormier

► To cite this version:

Luciana Maria Bortoluci Ormastroni, Inmaculada Lopez-Galilea, Julian Pistor, Benjamin Rutttert, Carolin Körner, et al.. Very high cycle fatigue durability of an additively manufactured single-crystal Ni-based superalloy. *Additive Manufacturing*, 2022, 54, pp.102759. 10.1016/j.addma.2022.102759 . hal-03871098

HAL Id: hal-03871098

<https://hal.science/hal-03871098>

Submitted on 25 Nov 2022

HAL is a multi-disciplinary open access archive for the deposit and dissemination of scientific research documents, whether they are published or not. The documents may come from teaching and research institutions in France or abroad, or from public or private research centers.

L'archive ouverte pluridisciplinaire **HAL**, est destinée au dépôt et à la diffusion de documents scientifiques de niveau recherche, publiés ou non, émanant des établissements d'enseignement et de recherche français ou étrangers, des laboratoires publics ou privés.

Very high cycle fatigue durability of an additively manufactured single-crystal Ni-based superalloy

Luciana Maria Bortoluci Ormastroni^{1,*}, Inmaculada Lopez-Galilea², Julian Pistor³, Benjamin Ruttert², Carolin Körner³, Werner Theisen², Patrick Villechaise¹, Fernando Pedraza⁴, and Jonathan Cormier^{1,*}

¹Institut Pprime, UPR CNRS 3346, Physics and Mechanics of Materials Department, ISAE-ENSMA, 1 avenue Clément Ader, BP 40109, 86961 Futuroscope-Chasseneuil Cedex, France.

²Ruhr-Universität Bochum, Institut für Werkstoffe, Lehrstuhl Werkstofftechnik, Universitätsstr. 150, D-44801 Bochum, Germany.

³Friedrich-Alexander-Universität Erlangen-Nürnberg, Department Werkstoffwissenschaften, Lehrstuhl für Werkstoffwissenschaften, Martensstr. 5, D-91058 Erlangen, Germany.

⁴Université de La Rochelle, Laboratoire des Sciences de l'Ingénieur pour l'Environnement (LaSIE UMR-7356 CNRS), Avenue Michel Crépeau, 17042 La Rochelle, cedex 01 – France

*Corresponding authors: luciana-maria.bortoluci-ormastroni@ensma.fr, jonathan.cormier@ensma.fr

Highlights

- Additively manufactured and Bridgman solidified CMSX-4 superalloy have comparable VHCF life under high temperature.
- The superalloy chemistry controls the fatigue life of defect-free specimens.
- Defect-free specimens fails by surface crack initiation.
- The fatigue limit is controlled by the superalloy oxidation resistance at temperature of 1,000 °C.

Abstract

A single crystalline (SX) nickel-based superalloy additively manufactured (AM) by electron beam-based powder bed fusion (PBF-E) was investigated under very high cycle fatigue (VHCF) at 1,000 °C in fully reversed conditions ($R_e = -1$). Specimens processed using a classical Bridgman solidification route and the impact of a hot isostatic pressing (HIP) treatment were also considered. It is shown that the fatigue lifetime of the AM specimens is higher or in the same range of the Bridgman processed ones with the same chemical composition. All defect-free AM samples fail by surface initiation with very long VHCF lives. In the absence of metallurgical defects such as grain boundaries or pores, the superalloy chemical stability against oxidation governs VHCF failure.

Keywords: Nickel-based superalloys, additive manufacturing, electron beam-based powder bed fusion, very high cycle fatigue.

35 **1 Introduction**

36 Nickel-based superalloys in single-crystalline (SX) form are widely used in the hot-sections of aero-engines for
37 the manufacturing of blades and vanes thanks to their excellent mechanical properties at temperatures up to ≈ 90
38 % of the material's melting temperature [1,2]. During service operations at (very) high temperatures, these
39 components undergo a variety of damages including creep, corrosion, and oxidation [2–4]. The entire replacement
40 of damaged components results in material and time costs. The use of additive manufacturing (AM) techniques
41 allows for the design of turbine blades with complex geometrical designs (e.g., intricate cooling channels)
42 combined with the possibility of refurbishment. Electron beam based powder bed fusion (PBF-E) is one of the
43 methods that can be adopted by the industry in the near future [5]. One of the most promising interests in employing
44 PBF-E to produce Ni-based SX superalloys is to control different processing parameters to obtain a superalloy
45 with specific microstructural characteristics [6].

46 CMSX-4 is one of the “legacy” Ni-based SX superalloys used in the hottest-sections of civil and military aero-
47 engines as blade material [1,7,8]. It is a γ/γ' superalloy which presents a quite high degree of chemical segregation
48 after casting compared to first generation Ni-based SX superalloys. A specific full heat treatment (HT) with
49 subsequent aging(s) (AG) is required to obtain a desired γ' size and volume fraction so as to optimize mechanical
50 properties, especially monotonic ones [6,9–11]. A collaboration between Cannon-Muskegon, the producer of
51 CMSX-4 alloy, and the research center SFB/TR 103 [12] allows SFB/TR 103 to reproduce this superalloy
52 chemistry for the subsequent preparation of SX PBF-E bars.

53 Considering that fatigue is responsible for most of the crack initiation events/failure cases of internally cooled
54 blades of aero-engines [13], it is of utmost importance to investigate fatigue properties of a PBF-E processed SX
55 superalloy, especially in the very high cycle fatigue (VHCF) regime in view of using such a processing route for
56 the manufacturing of Ni-based SX airfoils in future aero-engines. Fatigue tests under high and very high
57 temperatures with a lifetime higher than 10^8 cycles are very time consuming using a conventional fatigue machine
58 (≈ 100 Hz). Ultrasonic machines (in the kHz regime) became a solution in order to study the damage mechanisms
59 at very high vibratory frequencies [14]. It is also recalled that HCF/VHCF durability is a certifying criteria of
60 airfoils according to airworthiness authorities (e.g. EASA and FAA) [15–17], as the loading by vibratory stresses
61 turns out to be a matter of safety requirement of aero-engines.

62 From the authors' very best knowledge, there is only one published study focused on the fatigue properties of a
63 PBF-E SX superalloy in the low cycle fatigue (LCF) regime [9]. In fact, Meid et al. investigated the PBF-E SX
64 performance of CMSX-4 alloy in stress-controlled LCF at 950 °C/ 0.25 Hz and $R_\sigma = 0.6$ [9]. It was shown in this
65 pioneering study that the PBF-E SX alloy can perform similar to the conventionally processed SX alloy, provided
66 that an adequate heat treatment sequence is performed after the AM process. This result is not surprising
67 considering the fact that in such LCF conditions (high temperature, high mean stress, low frequency), a pronounced
68 cyclic ratcheting is observed, indicating that creep damage is also contributing to the overall LCF durability [9].

69 In contrast, the present paper focuses on the durability of the same PBF-E SX alloy in the VHCF domain at high
70 temperature/ $R_\epsilon = -1$. In such conditions, the VHCF life of conventionally processed Ni-based SX superalloys is
71 known to be highly dependent on the solidification parameters [14–20]. In fact, VHCF crack initiation occurs at
72 the largest casting pores in nearly 95 % of the cases at $R_\epsilon = -1/1000$ °C [15,17,19,20] and only occasionally at the

73 surface due to oxidation [15,19,21,22] or due to a prior plastic deformation, inducing surface recrystallization [23].
 74 VHCF life in fully reversed conditions at high temperature is hence really sensitive to the presence of defects such
 75 as pores and/or grain boundaries. In the absence of large solidification pores in the PBF-E material due to the AM
 76 process itself [24,25], a better fatigue performance is expected and/or different crack initiation mechanisms, but
 77 this needs to be investigated and therefore, it constitutes the main objective of this manuscript.

78 To achieve this aim, the PBF-E CMSX-4 SX samples have been tested with and without hot isostatic pressing
 79 (HIP) treatment [15,25,26] in the present investigation. The results were compared with the database available
 80 from the literature [15] using a Bridgman-processed CMSX-4 alloy after full HT, established using the same VHCF
 81 set-up.

82

83 2 Materials and methods

84 2.1. Chemical composition and heat treatments

85 The nominal chemical compositions of CMSX-4/Bridgman, ERBO/1 and CMSX-4 atomized powder used to build
 86 PBF-E specimens is listed in **Table 1**.

87 **Table 1**

88 CMSX-4/Bridgman, ERBO/1, and CMSX-4 atomized powder nominal chemical compositions (in wt. pct.).

Alloy	Ni	Cr	Mo	Co	W	Re	Al	Ti	Ta	Hf
CMSX-4/Bridgman [15]	Bal.	6.5	0.6	9.0	6.0	3.0	5.6	1.0	6.35	0.1
ERBO/1 [27]	Bal.	6.2- 6.6	0.5- 0.7	9.3- 10.0	6.2- 6.6	2.8- 3.1	5.4- 5.75	0.9- 1.1	6.3- 6.75	0.07- 0.12
CMSX-4 Atomized powder [31]	Bal.	6.6	0.6	9.9	6.4	2.9	6.2	1.1	6.6	0.08

89

90 The CMSX-4/Bridgman fatigue results are extracted from the literature [15]. For this reason, the HT was described
 91 in the previous article [15]. The ERBO/1 plate used to machine the fatigue specimens was provided by Doncasters
 92 Bochum company in partnership with the Ruhr-Universität Bochum. This plate had a 20 mm thickness. The HT
 93 (ERBO/1C according to [27]) was presented in the literature [27].

94 Square bars with 12 mm edges were built (**Fig.1 a**) by the PBF-E method. The PBF-E CMSX-4 SX samples were
 95 divided in two different groups depending on whether they have or not a HIP treatment. First, the AM/HT/REC
 96 (AM: Additive manufacturing, HT: Heat treated, REC: Recycled atomized powder) specimens were built with
 97 recycled powder, HT by standard method in air at 1,315 °C/35 min and finally aged at 1,140 °C/2 h/AQ (air
 98 quench) and at 870 °C/20 h/AQ. The AM/HIP (HIP: HIP treatment) specimens were homogenized in the QIH-9
 99 HIP (hot isostatic pressing) at 1,315 °C/35 min under 100 MPa Argon pressure. The material was directly quenched
 100 after holding by applying the fast-cooling capability of the HIP set-up to achieve ultrafine γ precipitates. Then, the

101 material was subjected to the same AG treatment as defined for the non-HIPed material. The AM/HIP samples
 102 were received in two different batches. The first batch containing eight bars had been built using recycled powder
 103 (AM/HIP/REC). The second batch contained four bars fabricated with fresh powder (AM/HIP/FRS) (FRS: Fresh
 104 atomized powder). The nomenclature is detailed in **Table 2**.

105 **Table 2**

106 Sample's nomenclature. HT is the denomination for full heat treatment. PBF-E is the denomination for electron
 107 beam based powder bed fusion. SHT is the denomination for solution heat treatment. AG is the denomination for
 108 aging treatment. AQ is the denomination for air quench. HIP is the denomination for hot isostatic pressing.

Nomenclature	Superalloy/Solidification process/Heat treatment
CMSX-4/Bridgman	CMSX-4 solidified by classical Bridgman method → HT described in the literature [15]
ERBO/1	ERBO/1 solidified by classical Bridgman method → HT described in the literature as ERBO/1C [27]
AM/HT/REC	Additive manufacturing (PBF-E) samples built w/ recycled CMSX-4 atomized powder → SHT in air at 1,315 °C/35 min and AG steps at 1,140 °C/2 h/AQ and 870 °C/20 h/AQ
AM/HIP/REC	Additive manufacturing (PBF-E) samples built w/ recycled CMSX-4 atomized powder → HIP homogenization at 1,315 °C/35 min under 100 MPa Argon pressure
AM/HIP/FRS	Additive manufacturing (PBF-E) samples built w/ fresh CMSX-4 atomized powder → HIP homogenization at 1,315 °C/35 min under 100 MPa Argon pressure

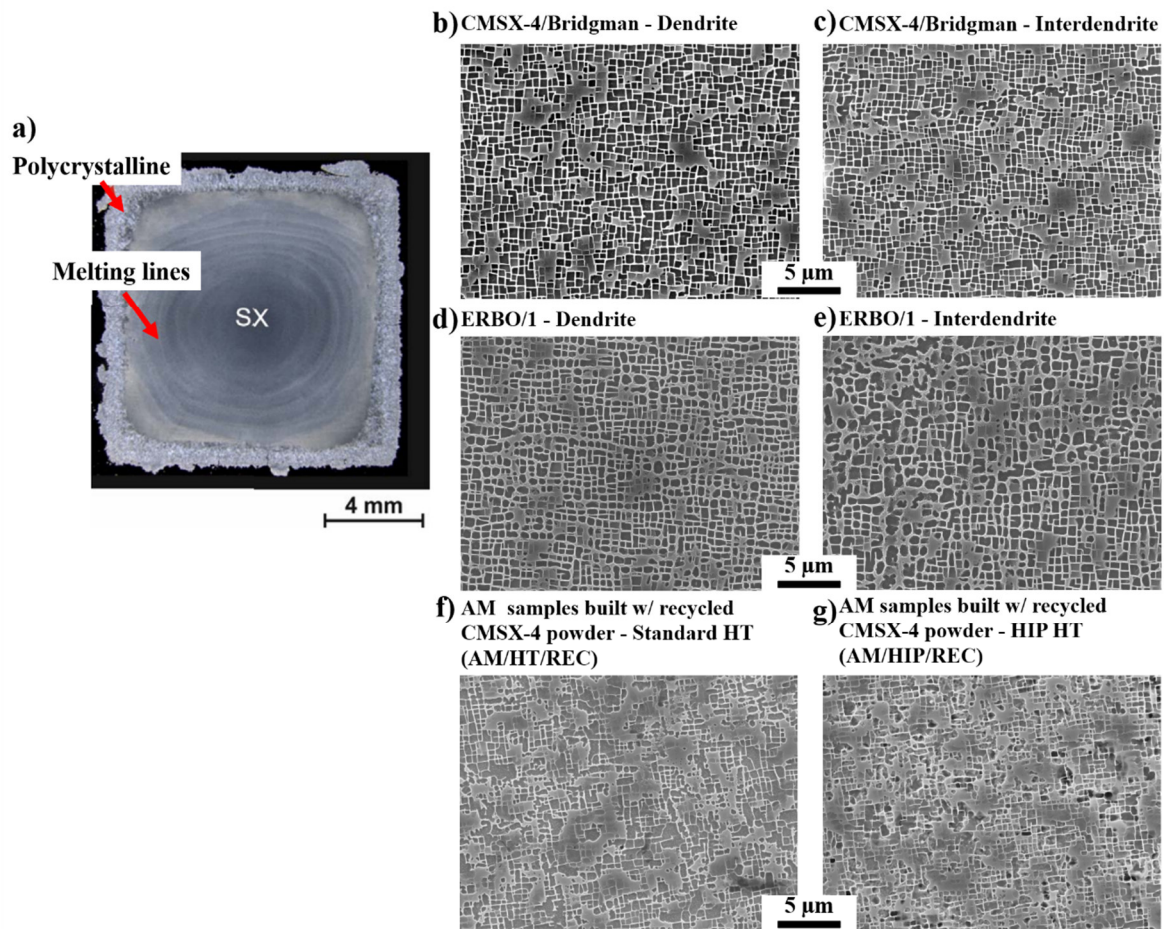
109

110 *2.2. Stereological analyzes*

111 A γ/γ' stereological analysis was performed using a JEOL JSM-7000F scanning electron microscope, by applying
 112 the secondary electron imaging (SEI) mode operating at 25 kV. The microstructures are shown in **Fig. 1 b-g**. The
 113 observations have been made in both primary dendrite arms (D) and interdendritic spacing (ID) for Bridgman
 114 processed CMSX-4/Bridgman and ERBO/1 alloys. As the PBF-E processed alloy has very small primary dendrite
 115 arms spacings [6,31], almost no remaining difference in precipitate size and morphology can be observed in a fully
 116 heat treated/HIPed state across this very fine dendritic structure (**Fig. 1 f-g**). The software ImageJ was employed
 117 to analyze the γ' size. All measurements were done in the dendrite core for Bridgman solidified alloys. The γ'
 118 average edge length of CMSX-4/Bridgman alloy is 590 ± 120 nm, and it is 560 ± 80 nm for the ERBO/1 one. The
 119 AM/HT/REC presents 420 ± 80 nm, and AM/HIP/REC 470 ± 100 nm sizes. The average edge length of γ'
 120 precipitates in the PBF-E SX is hence smaller compared to the one in CMSX-4/Bridgman and ERBO/1 materials.
 121 This difference in γ' size between all the investigated specimens has been neglected in the following of this article
 122 since it is known from the prior literature that the VHCF properties of Ni-based SX superalloys are not dependent
 123 on the precipitation size and morphology at $R_e = -1/1000$ °C [17]. Moreover, a possible small variation in γ' volume
 124 fraction around 70 % does not seem neither to have any impact on the VHCF properties in these conditions [15].

125 The CMSX-4 PBF-E SX stereological characterization detailed in [25,29,30] has shown that the SX part developed
126 pores having a $\approx 1.7 \mu\text{m}$ average diameter size [24,25], which contrasts with the Bridgman method that results in
127 solidification pores of up to $200 \mu\text{m}$ after the complete solution heat treatment (SHT) for this alloy [28].

128



129

130 **Fig. 1.** (a) PBF-E SX 12 mm square bars microstructure details (aqua regia etched). (b) γ/γ' microstructure of
131 CMSX-4/Bridgman observed in primary dendrite arms and (c) in interdendritic spacing. (d) ERBO/1 alloy
132 solidified by a Bridgman method in primary dendrite arms and (e) in interdendritic spacing. (f) CMSX-4 alloy
133 processed by PBF-E after standard heat treatment and (g) after HIP treatment.

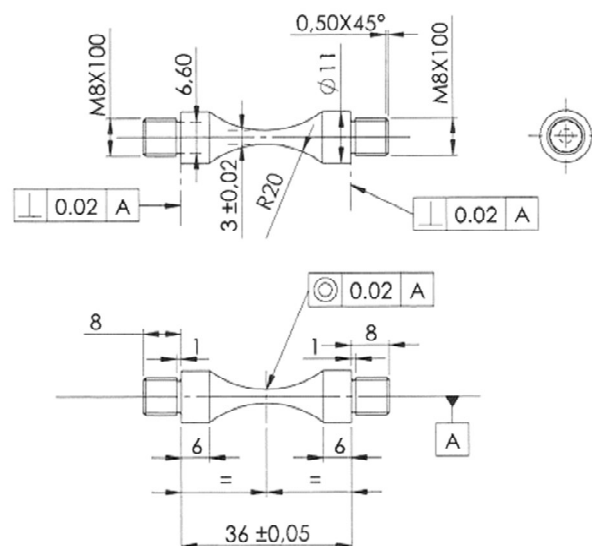
134

135 2.3. Specimens' machining and very high cycle fatigue tests details

136 VHCF tests were performed using hourglass-shaped samples (see **Fig. 2**) [32]. The samples were extracted by
137 electric discharge machining and subsequent turning to reach the final shape. Two samples for AM/HT/REC,
138 twelve samples for AM/HIP of the two batches (8 specimens AM/HIP/REC and 4 specimens AM/HIP/FRS) and
139 eight samples for ERBO/1 were machined at Pprime Institute. A thickness of 0.2 mm from the original diameter
140 was first removed by SiC grinding to remove residual stresses inherited from the machining steps. This polishing
141 step was essential to avoid surface recrystallization during the fatigue tests at high temperature. Thereafter, the

142 surfaces were gently ground and polished to a final mirror polish (1 μm diamond suspension) with the final steps
143 parallel to the loading axes.

144 Strain-controlled VHCF tests were performed at 1,000 $^{\circ}\text{C}$ (± 2 $^{\circ}\text{C}$), $f = 20 \pm 0.5$ kHz, $R_e = -1$ with an ultrasonic
145 fatigue machine used in previous studies [16–19,21,23,32]. The fatigue tests were performed with a sinusoidal
146 waveform. These tests were performed using alternating stresses allowing i) a direct comparison with
147 conventionally processed Ni-based single crystalline specimens previously tested at Institut Pprime [16–
148 19,21,23,32], ii) a good control of specimen's temperature and iii) failure of specimens in a reasonable time. An
149 induction coil was used as a heating source, the power of which was controlled by a closed loop with a dual-
150 wavelength pyrometer measuring the specimen's central temperature. A pre-heating of 45 min at 1,000 $^{\circ}\text{C}$ was
151 applied before starting the tests to stabilize the surface oxides and resulting surface emissivity. Due to the high
152 density of dislocations stored in the AM processed specimens, especially in the HIPped ones, only low alternating
153 stresses were used to limit the impact of specimens' self-heating on their temperature control. Hence, AM
154 specimens were all tested with an alternating stress σ_a below 180 MPa. With this high temperature VHCF set-up
155 used in these previously described conditions, fluctuations in alternating stress of ± 3 MPa at maximum have
156 been observed throughout tests.



157

158 **Fig. 2.** Ultrasonic fatigue sample dimensions (in mm), used for VHCF tests at 1,000 $^{\circ}\text{C}$.

159

160 2.4. Post-mortem analyses

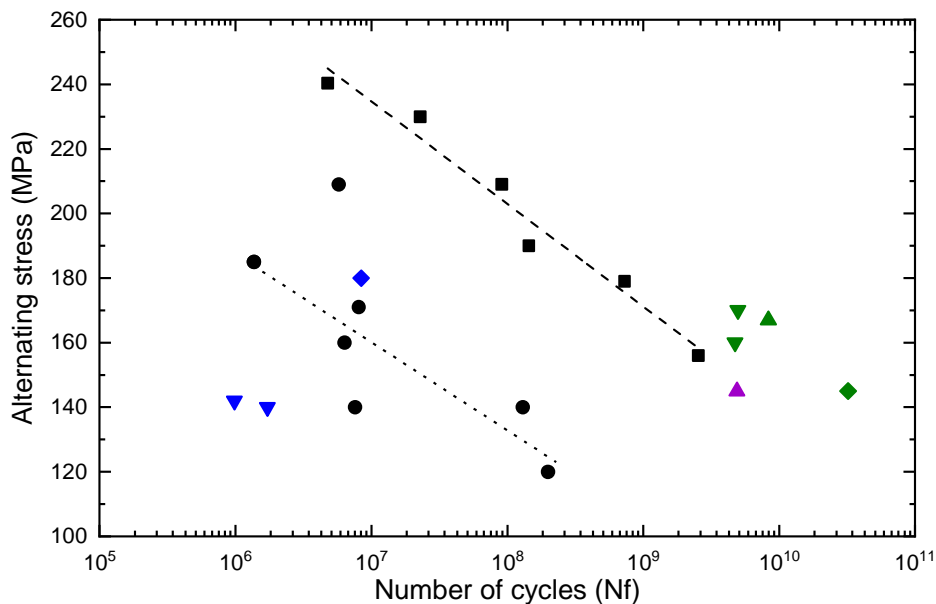
161 Optical and scanning electron microscopy (OM and SEM, respectively) were employed to perform post-mortem
162 observations. Fractographic analyses were carried out using a field emission gun (FEG) microscope JEOL JSM-
163 7000F operating at 25 kV. The longitudinal sections were mirror polished down to 1 μm to observe the
164 microstructure under secondary (SEI) and backscattered electrons (BSE) imaging modes in the same equipment
165 operating at ≈ 10 mm work distance. The chemical analyses were conducted with an EDAX energy dispersive
166 spectrometer (EDS). The analyses were made on un-etched surfaces to avoid any potential dissolution of oxides,
167 carbides and other metallurgical phases that could fake the interpretation. In addition, electron backscatter

168 diffraction (EBSD) analyses were performed to characterize the crystallographic orientation around the internal
 169 crack initiation. It was performed using a second JEOL JSM-6100 SEM, operating at 25 kV, and the orientation
 170 imaging microscopy (OIM) software EDAX, version 6.1. A 0.2 μm scanning step was chosen. The specimens
 171 were polished using colloidal silica solution (particle size 0.04 μm).

172 3 Results

173 3.1. VHCF performances and fractographic analyses

174 The alternating stress (σ_a) as a function of the number of cycles to failure (Nf) diagram gathering all VHCF results
 175 obtained in the present study is presented in **Fig. 3**. It can also be observed that fatigue lives ranging from $\approx 10^6$
 176 cycles up to $\approx 3.0 \times 10^{10}$ cycles have been obtained at $\sigma_a = 145$ MPa. The latter is probably the longest fatigue test
 177 ever performed on this class of alloy at high temperature. Significant scattering in ERBO/1 can result from different
 178 crack initiation mechanisms that will be detailed later in this article.



Symbol: Superalloy

- CMSX-4/Bridgman [15]
- ERBO/1
- ◆ AM samples built w/ recycled CMSX-4 atomized powder
→Standard HT (**AM/HT/REC**)
- ▲ AM samples built w/ recycled CMSX-4 atomized powder
→HIP HT(**AM/HIP/REC**)
- ▼ AM samples built w/ fresh CMSX-4 atomized powder
→HIP HT(**AM/HIP/FRS**)

Color: Crack initiation mode

- Solidification pore
- High angle grain boundary
- Bulk
- Surface

Trend line

- - - CMSX-4/Bridgman
- · · · ERBO/1

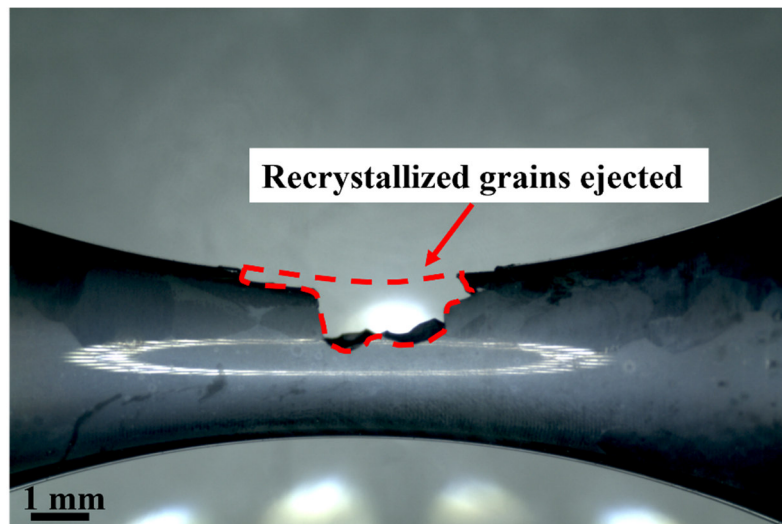
179

180 **Fig. 3.** S-N diagram at 1,000 °C, $R_\epsilon = -1$ / $f = 20$ kHz. The alternating stress σ_a is plotted as a function of the
 181 number of cycles to failure. The CMSX-4/Bridgman data, represented with black squares, were extracted from the
 182 literature [15]. (For interpretation of the references to color in this figure legend, the reader is referred to the web
 183 version of this article.)

184

185 The AM processed specimens present very different VHCF lives, either very long ones in excess of 5.0×10^9
186 cycles, or short ones below 10^7 cycles. In fact, six AM/HIP/REC samples failed from stray grains, which
187 presumably formed during the PBF-E and/or HIPing processes. The presence of such grains within the gauge part
188 of VHCF specimens, especially close to the surface, results in very low VHCF lives. Failure during the initial
189 ramping-up in alternating stress up to reaching the desired value in σ_a even occurred in six different samples
190 containing stray grains (**Fig. 4** and **Table 3**). These tests were considered as “unsuccessful” since no stabilized
191 alternating stress was reach.

192



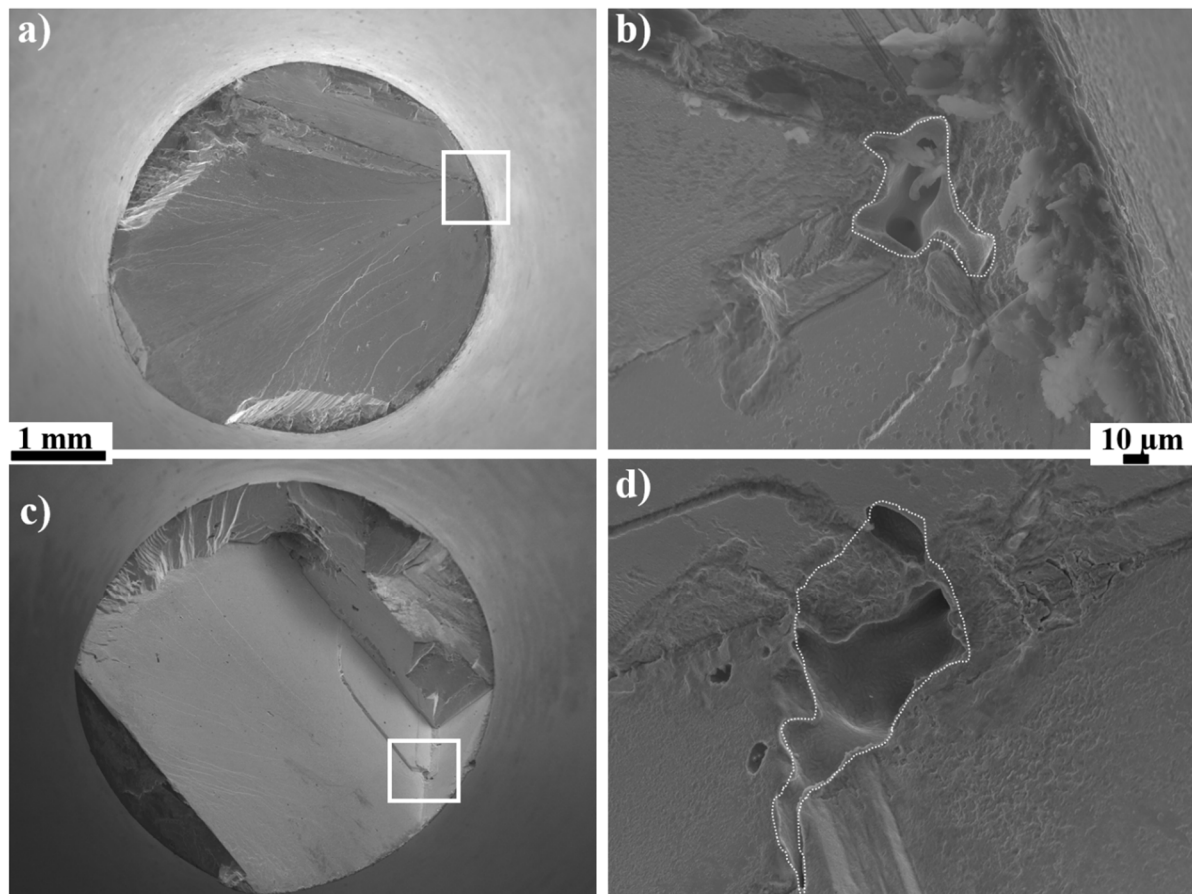
193

194 **Fig. 4.** Optical microscope observations of two AM/HIP/REC samples that presented immediate failure. The red
195 dotted region illustrates the location of a recrystallized grains ejected from the specimen gauge part during the
196 application of the alternating stress.

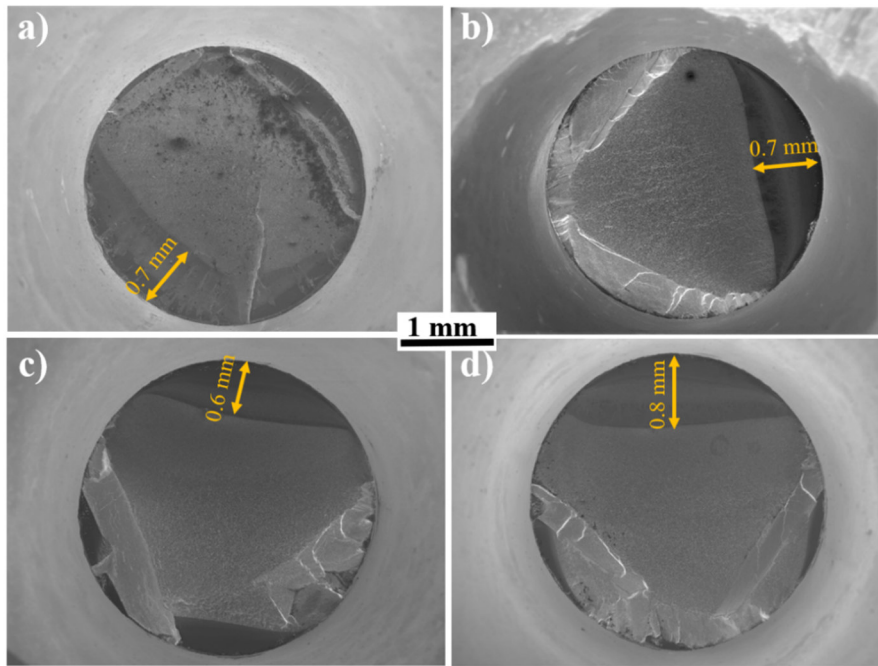
197 All other successful tests using PBF-E processed specimens (i.e., AM/HT/REC, AM/HIP/REC and AM/HIP/FRS
198 samples) with a few cycles close to the CMSX-4/Bridgman trend line failed from a surface crack initiation or from
199 an internal site (see **Fig. 3**). The presence of grain boundaries within the gauge part of specimens appears to be
200 detrimental to the VHCF life of AM processed specimens and may lead to fatigue lives well below the ones
201 obtained for Bridgman processed alloys (see **Fig. 3** and **Table 3**).

202 After mechanical testing, fractographic observations were performed. The fracture analysis of CMSX-4/Bridgman
203 specimens was already presented in detail by Cervellon et al. [15]. Crack initiation from internal solidification
204 pores was systematically obtained, these critical pores having a maximum diameter ranging from 50 to 150 μm
205 [15]. In good agreement with this reference database, ERBO/1 specimens systematically presented a crack
206 initiation from solidification pores with a size ranging from 80 to 200 μm (see **Table 3** and **Fig. 5**). Such a crack
207 initiation mode has already been well explained in the literature [15,20,32]. The quite pronounced scatter in VHCF
208 life of ERBO/1 specimens displayed in **Fig. 3** results from the quite large variation in casting pore size serving as
209 the main crack initiation site (**Fig. 5**), since specimens were machined out from a thick SX plate. In fact, using the
210 same casting parameters, large SX castings are known to introduce larger solidification pores, overall reducing the
211 VHCF life [15]. Hence, the variability in VHCF life of ERBO/1 does not deserve further analysis/discussion.

212 Focusing on the successful results shown in **Fig. 3** for PBF-E-processed specimens (i.e., no consideration of
213 specimens containing high angle grain boundaries), most of AM/HT/REC, AM/HIP/REC and AM/HIP/FRS
214 samples presented crack initiation at the surface, as shown in **Fig. 6**. According to **Fig. 6**, surface cracks assisted
215 by oxidation as deep as 0.8 mm have been observed after failure. The fracture surfaces of these specimens are also
216 characterized by a subsequent crack propagation zone in mode I (highlighted by yellow dotted lines), which seems
217 to be less oxidized according to the lighter contrast, and then by a final failure area in shear mode. Specimens with
218 a high VHCF life ($N_f > 4 \times 10^9$ cycles) presented several surface cracks (secondary cracks) that were perpendicular
219 and parallel to the main loading axis, as shown in **Fig. 7** for two different specimens tested at $\sigma_a = 145$ MPa. Both
220 specimens present a non-negligible density of surface cracks. However, the main crack initiation site was not
221 necessarily at the specimen's surface (see **Table 3** and **Fig. 8a**). In fact, only one specimen had crack initiation
222 from an internal site (AM/HIP/REC-2, see **Fig. 8b**) with the characteristic rough zone commonly observed around
223 the main crack initiation site of samples tested under VHCF conditions [15,20], see yellow insert in **Fig. 8b**.
224 However, it was not possible to unambiguously conclude on the nature this crack initiation site from fractographic
225 observations and further observations along longitudinal cuts were thus performed.



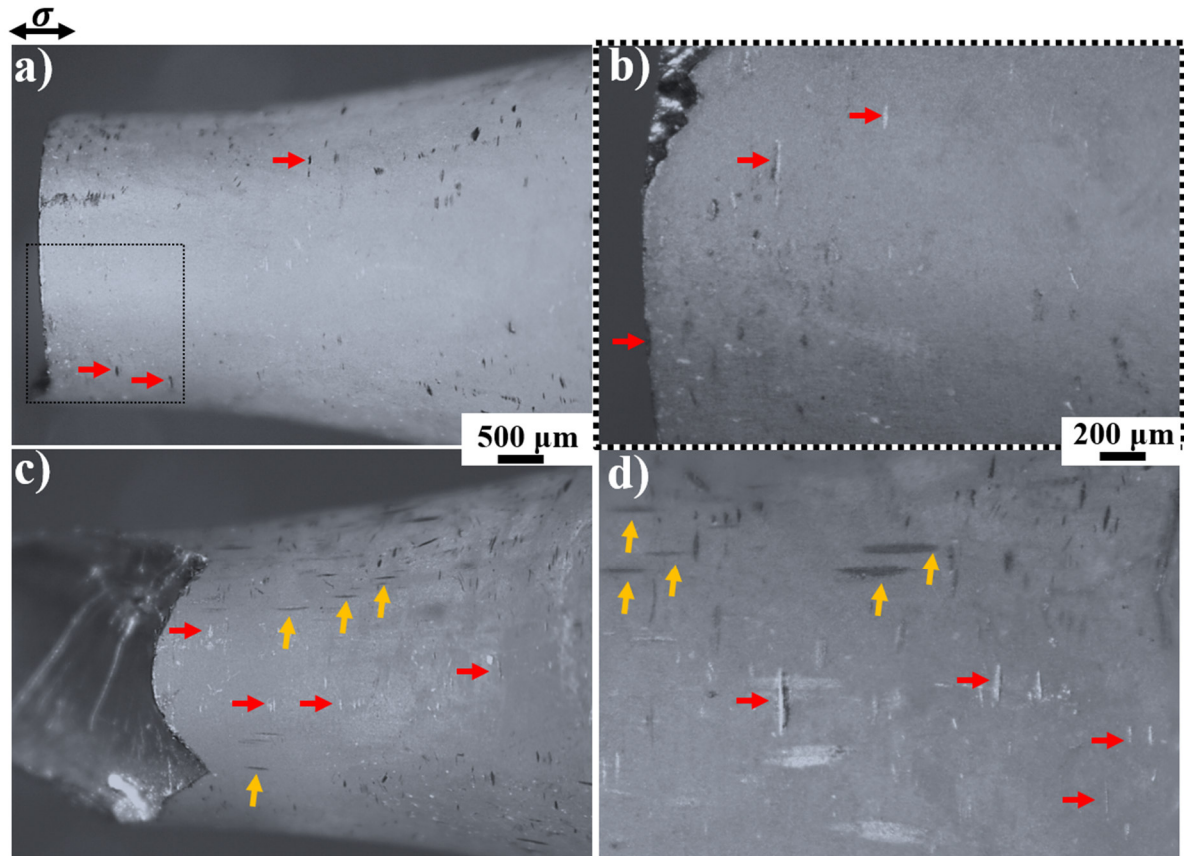
226
227 **Fig. 5.** Fractographic observations of ERBO/1 samples with main crack initiation from solidification pores. (a)
228 ERBO/1-6 ($\sigma_a = 209$ MPa, with $N_f = 5.7 \times 10^6$ cycles) and (b) crack zone magnification, detail to the presence of
229 a casting pore close to the surface with diameter of ≈ 40 μm . (c) ERBO/1-1 ($\sigma_a = 160$ MPa, with $N_f = 6.6 \times 10^6$
230 cycles) and (d) crack zone magnification, detail to the presence of a casting pore with diameter of ≈ 170 μm .



231

232 **Fig. 6.** Fractographic observations of PBF-E processed specimens with main crack initiation from the surface: (a)
233 AM/HT/REC-1 ($\sigma_a = 145$ MPa, $N_f = 3.2 \times 10^{10}$ cycles), (b) AM/HIP/REC-1 ($\sigma_a = 167$ MPa, $N_f = 8.3 \times 10^9$ cycles),
234 (c) AM/HIP/FRS-2 ($\sigma_a = 170$ MPa, $N_f = 4.9 \times 10^9$ cycles), (d) AM/HIP/FRS-3 ($\sigma_a = 160$ MPa, $N_f = 4.7 \times 10^9$
235 cycles). The maximum depth of the main fatal crack initiated at the surface is added for each specimen.

236



237

238 **Fig. 7.** Two examples of PBF-E processed specimens with surface cracks. (a and b) AM/HT/REC-1 and (c and d)
 239 AM/HIP/REC-2. Both tests were performed at $\sigma_a = 145$ MPa, with $N_f = 3.2 \times 10^{10}$ cycles for AM/HT/REC-1 and
 240 $N_f = 4.9 \times 10^9$ cycles for AM/HIP/REC-2. Red and yellow arrows indicate, respectively, cracks perpendicular and
 241 parallel to the loading axis. (For interpretation of the references to color in this figure legend, the reader is referred
 242 to the web version of this article.)

243

244

245

246

247

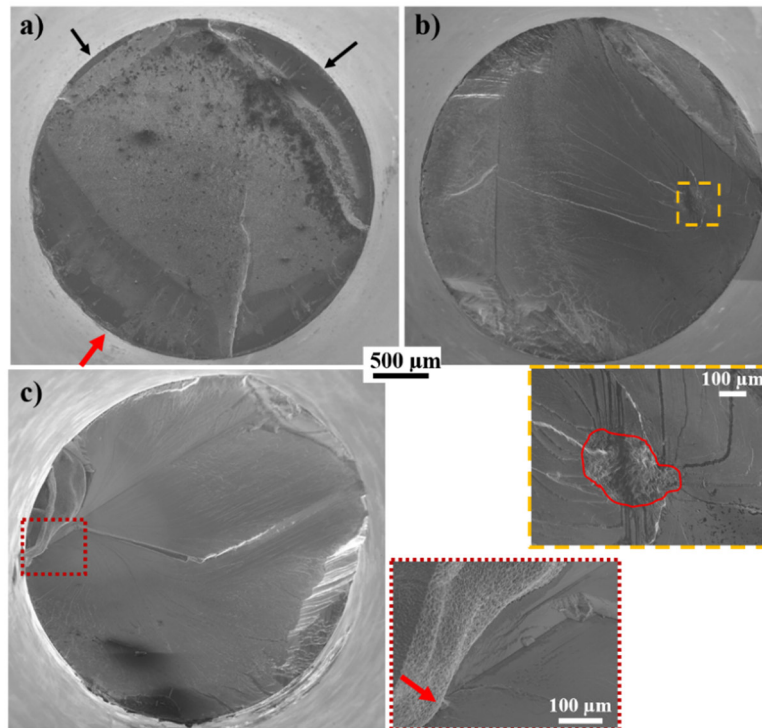
248

249

250

252 VHCF results at 1,000°C/ $R_e = -1/f = 20$ kHz of Bridgman and PBF-E processed ERBO/1 SX specimens.

	Specimen	σ_a (MPa)	Nf (cycles)	Crack initiation	
PBF-E	AM/HT/REC-1	145	3.2×10^{10}	Surface initiation	
	AM/HT/REC-2	180	8.4×10^6	High angle grain boundary	
	AM/HIP/REC-1	167	8.3×10^9	Surface initiation	
	AM/HIP/REC-2	145	4.9×10^9	Bulk initiation	
	AM/HIP/REC-3			Immediate failure during alternating stress ramp-up	
	AM/HIP/REC-4			Immediate failure during alternating stress ramp-up	
	AM/HIP/REC-5			Immediate failure during alternating stress ramp-up	
	AM/HIP/REC-6			Immediate failure during alternating stress ramp-up	
	AM/HIP/REC-7			Immediate failure during alternating stress ramp-up	
	AM/HIP/REC-8			Immediate failure during alternating stress ramp-up	
	AM/HIP/FRS-1	142	9.8×10^5	High angle grain boundary	
	AM/HIP/FRS-2	170	4.9×10^9	Surface initiation	
	AM/HIP/FRS-3	160	4.7×10^9	Surface initiation	
	AM/HIP/FRS-4	140	1.7×10^6	High angle grain boundary	
	Bridgman	ERBO-BR-1	160	6.3×10^6	Solidification pore
		ERBO-BR-2	140	7.6×10^6	Solidification pore
ERBO-BR-3		120	1.9×10^8	Solidification pore	
ERBO-BR-4		171	8.0×10^6	Solidification pore	
ERBO-BR-5		140	1.3×10^8	Solidification pore	
ERBO-BR-6		209	5.7×10^6	Solidification pore	
ERBO-BR-7		185	1.3×10^6	Solidification pore	
ERBO-BR-8		185	2.6×10^7	Solidification pore	



254

255 **Fig. 8.** Fractographic observations of three PBF-E processed specimens: (a) AM/HT/REC-1 ($\sigma_a = 145$ MPa, $N_f =$
 256 3.2×10^{10} cycles) with surface crack initiation pointed by the arrows, the main initiation is highlighted by the red
 257 arrow; (b) AM/HIP/REC-2 ($\sigma_a = 145$ MPa, $N_f = 4.9 \times 10^9$ cycles) with a main internal crack site, presenting the
 258 characteristic rough zone pointed by the dotted yellow square (see insert); and (c) AM/HIP/FRS-1 ($\sigma_a = 142$ MPa,
 259 $N_f = 9.8 \times 10^5$ cycles) with a main initiation from a surface grain boundary pointed by the red dotted square (see
 260 insert). (For interpretation of the references to color in this figure legend, the reader is referred to the web version
 261 of this article.)

262

263 3.2. Microstructure investigation along longitudinal sections

264 The longitudinal cross-sections were prepared in AM/HT/REC-1 and AM/HIP/REC-2 specimens to better
 265 understand crack initiation mechanisms for both PBF-E processed specimens.

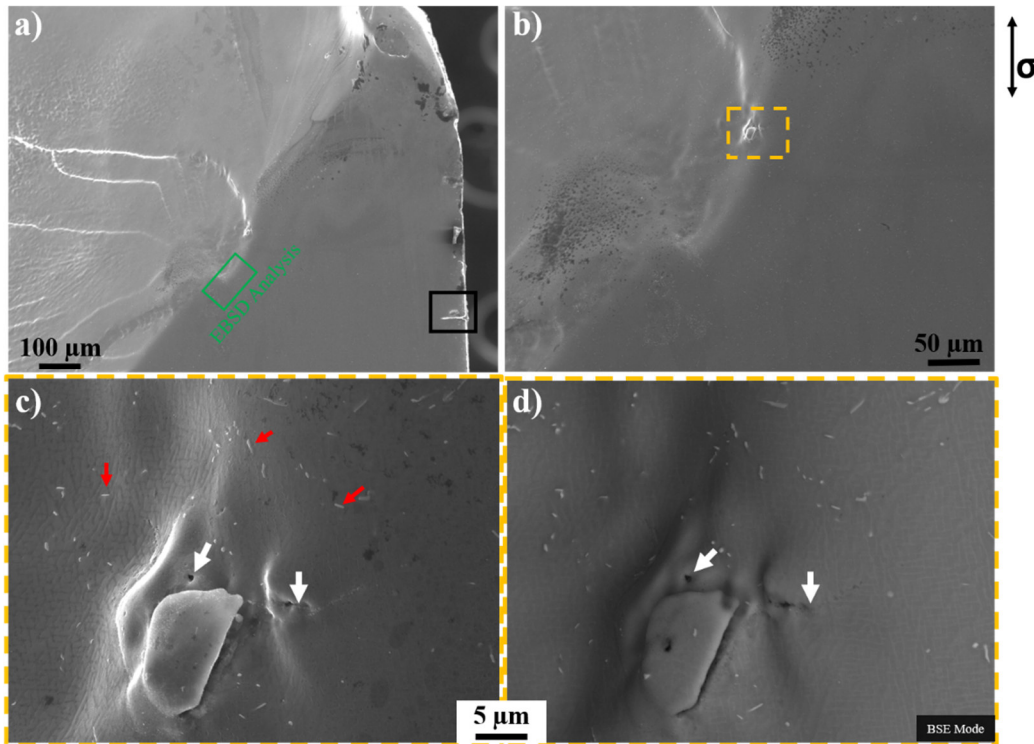
266

267 3.2.1. Crack initiation from an internal site: AM/HIP/REC-2 specimen

268 The crack initiation site observed in **Fig. 8b** has been investigated at a high magnification and along a longitudinal
 269 section intercepting the initiation site as shown in **Fig. 9**. Different imaging modes have been used to try to
 270 determine its exact nature. From this figure, it was possible to identify needle-shaped precipitates (red arrows in
 271 **Fig. 9 c**). The rough zone presented discontinuities that look very similar to vacancies as previously observed by
 272 Cervellon et al. [20] within the rough zone due to locally very high deformation magnitude (**Fig. 9 c and d**). These
 273 small pores whose size is below $1 \mu\text{m}$ may have also been inherited from the AM process.

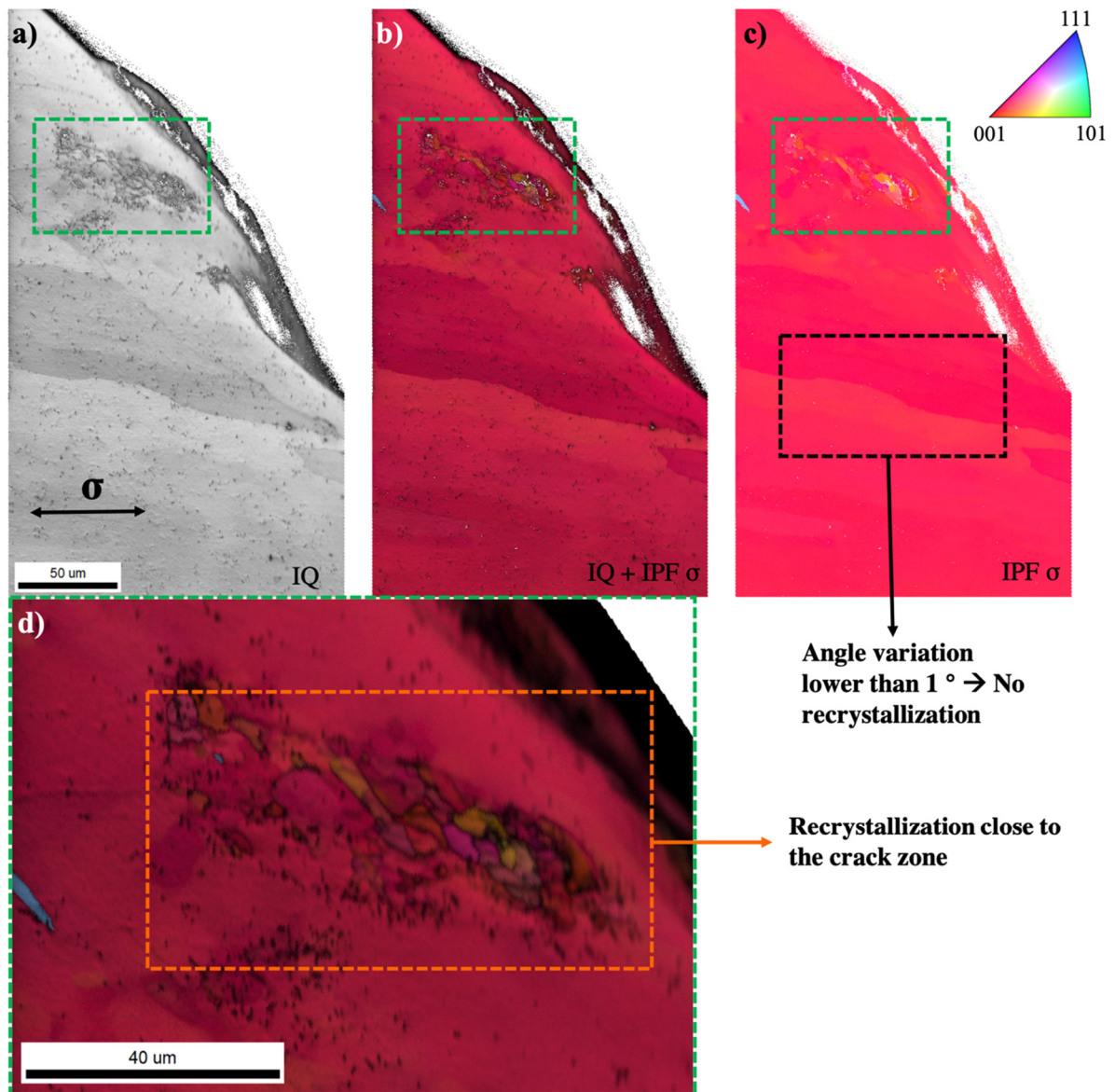
274 **Fig. 10** shows the EBSD analysis performed just below the crack initiation site according to the localization
 275 provide in **Fig. 9a** by the green rectangle. The IQ+IPF images show that most of this region below the crack

276 initiation site presents angular variations lower than 1° indicating the absence of recrystallization. However, a
277 small “recrystallization” zone of $\approx 60 \mu\text{m}$ in extension (see **Fig. 10d**) was observed close to the crack initiation
278 zone. It is composed a several low angle boundaries of local misorientation typically lower than 10° . The internal
279 stresses remaining from the melting lines combined with the HIP treatment can be the explanation of the
280 recrystallized zone indicated in **Fig. 10**.



281
282 **Fig. 9.** (a) Crack initiation site of AM/HIP/REC-2 ($\sigma_a = 145 \text{ MPa}$, $N_f = 4.9 \times 10^9$ cycles) observed along a
283 longitudinal section. Few secondary cracks are observed at the surface (see black square). (b) Crack initiation site
284 identified by the rough zone, (c) magnification images using the SEI and (d) BSE imaging mode. White arrow is
285 pointing out a remaining pore and red arrows highlight needle-shaped precipitates. The green square in (a) shows
286 the location where the EBSD analyses have been performed. (For interpretation of the references to color in this
287 figure legend, the reader is referred to the web version of this article.)

288



289

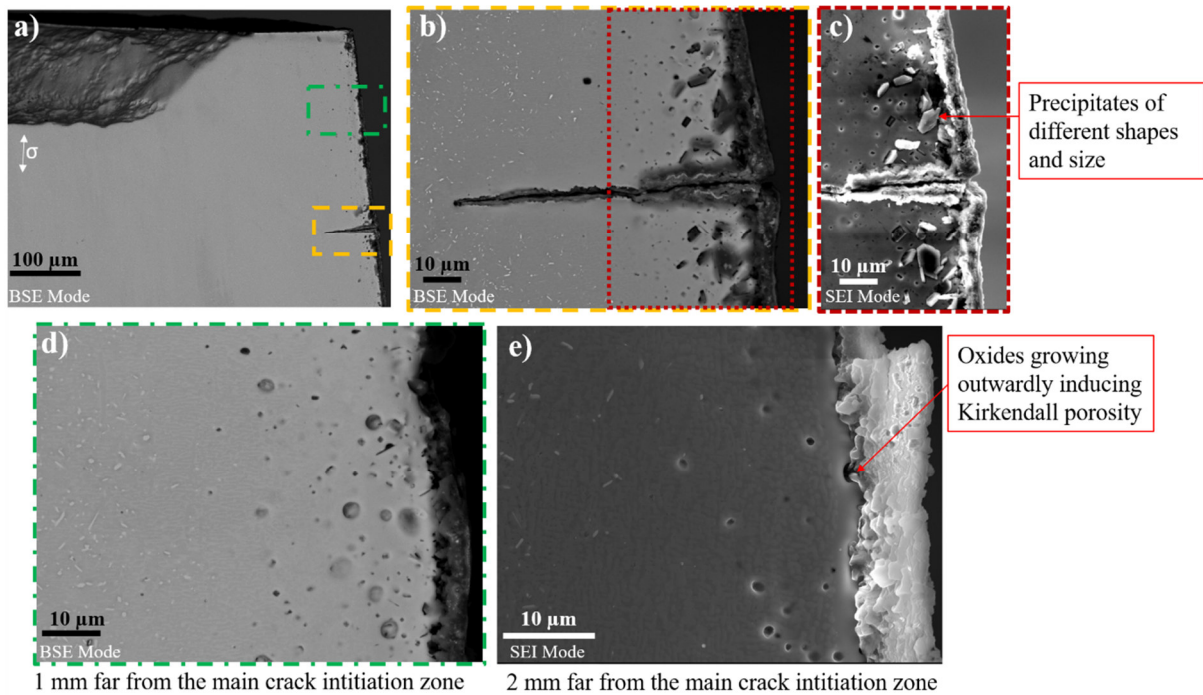
290 **Fig. 10.** EBSD characterization of AM/HIP/REC-2 ($\sigma_a = 145$ MPa, $N_f = 4.9 \times 10^9$ cycles) crack initiation zone
 291 (green square in **Fig. 9a**) including (a) image quality (IQ). (b) IQ and inverse pole figure (IPF), (c) and IPF relative
 292 to the loading direction. Angle variation lower than 1° is pointed by the black dotted square. A region (dotted green
 293 rectangles in (a-c)) containing several recrystallized cells with low angle grain boundaries is shown in (d). (For
 294 interpretation of the references to color in this figure legend, the reader is referred to the web version of this article.)

295

296 3.2.2. Crack initiation from the surface: AM/HT/REC-1 specimen

297 **Fig. 11** shows the features found along a longitudinal section of the AM/HT/REC-1 specimen. Failure from surface
 298 initiation is only shown for the HT sample since the results obtained for AM/HIP/REC-1, AM/HIP/FRS-2 and
 299 AM/HIP/FRS-3 (**Fig.6** and **Table 3**) are equivalent. **Fig. 11a** illustrates the presence of a secondary crack whose
 300 depth is ≈ 70 μm . This crack seems to be filled by oxides up to its tip. **Fig. 11b** and **c** are observations in BSE and
 301 SEI modes, respectively, allowing to highlight significant features like the square-like precipitates around the crack
 302 initiation zone and the oxidation inside the crack. A ≈ 30 μm -thick layer with Kirkendall porosity and precipitates

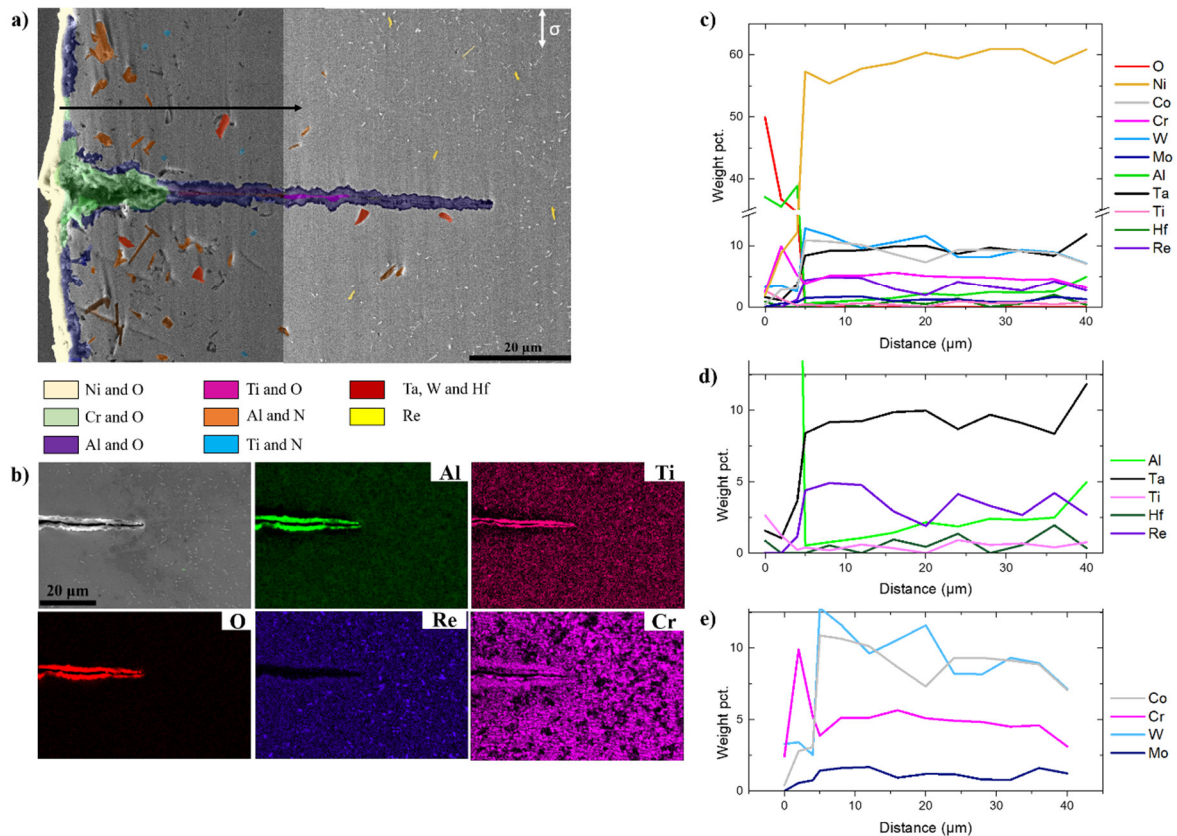
303 of different shapes appear underneath the surface (**Fig.11 d** and **e**). **Fig. 11e** illustrates the oxides growing
 304 outwardly and leaving behind Kirkendall voids. None of these particular features were previously observed either
 305 in CMSX-4/Bridgman in VHCF at 1,000 °C by Cervellon et al. [15] or in the CMSX-4 PBF-E samples after LCF
 306 tests at 950 °C by Meid et al. [6], probably due to shorter duration of the tests.
 307



308
 309 **Fig. 11.** Microstructure characterizations of AM/HT/REC-1 ($\sigma_a = 145$ MPa, $N_f = 3.2 \times 10^{10}$ cycles) along a
 310 longitudinal section: (a) high magnification overview of one side of the sample in BSE mode. (b) Secondary crack
 311 detail (orange dotted rectangle in (a)) in BSE mode and (c) SEI mode. (d) Surface detail (green dotted rectangle in
 312 (a)) 1 mm far from the main crack initiation site in BSE mode, and (e) 2 mm far from the main crack initiation
 313 zone in SEI mode. (For interpretation of the references to color in this figure legend, the reader is referred to the
 314 web version of this article.)

315
 316 **Fig. 12a** highlights the chemical elements that constitute the oxides and the precipitates. The external oxide scale
 317 outside the crack is mainly composed of O, Ni and Cr (light yellow and green). The internal crack oxides comprise
 318 Ti, Ta and Al (purple and dark pink). The needle-like precipitates are rich in Re (yellow) ≈ 20 wt. % (see also Re
 319 map in **Fig. 12b**), and several big precipitates are composed of Ta, W and Hf (red). The large square-shaped
 320 precipitates close to the surface are composed of N and Al (orange), and the small ones are composed of N and Ti
 321 (blue). Re-rich needle-shaped precipitates are probably TCP ones, presumably μ or P phases, based on their
 322 morphology and on their very high Re content [33].

323 The EDS composition profile of the oxide and the substrate is displayed in **Fig. 12b**. The oxide is divided in three
 324 main layers: an external NiO, an intermediate Cr_2O_3 and internal Al_2O_3 layers. Depletion of Al, Ta and Ti between
 325 the bulk and the surface is also observed (**Fig. 12c**), which results in the countercurrent increase in Re and W.



326

327 **Fig. 12.** AM/HT/REC-1 ($\sigma_a = 145$ MPa, $N_f = 3.2 \times 10^{10}$ cycles) EDS analysis. (a) SEI image artificially colored
 328 with the Photoshop software in agreement with the chemical elements X-ray maps analysis in (b). (b) X-ray maps
 329 of the crack tip highlighting the elements O, Al, Re, Ti, and Cr. (c) Chemical composition through the profile
 330 illustrated by the black arrow in **Fig. 12a** including all elements, (d) with a focus on Al, Ta, Ti, Hf, and Re elements
 331 and (e) with a focus on Co, Cr, W, Mo elements. (For interpretation of the references to color in this figure legend,
 332 the reader is referred to the web version of this article.)

333

334 4. Discussion

335 From the present experiments, it has been observed that PBF-E processed specimens performed extremely well in
 336 VHCF at $1,000$ °C/ $R_\epsilon = -1/f = 20$ kHz provided that they are defect-free, i.e., they are fully single crystalline.
 337 Moreover, in comparison to conventionally processed (Bridgman solidification) Ni-based SX superalloys, which
 338 usually present crack initiation from the largest casting pores in these conditions irrespective of the alternating
 339 stress (see **Figs. 3** and **5** and refs. [14–20,23]), nearly all defect-free PBF-E processed specimens failed from the
 340 surface, with a crack initiation process assisted by oxidation (see **Figs. 3, 6, 7a, 8a, 11** and **12**) and equivalent
 341 results for fresh and recycled atomized powder. Since only AM specimens failed from an internal site, one can
 342 hypothesize on a very high dislocation density at local scale inherited from the building/HIP processes (**Fig. 9** and
 343 **10**). Yet, further analyses and additional results with a similar crack initiation mechanism would be required to
 344 unambiguously assess this potential mechanism of crack initiation. In the previous literature investigating fatigue
 345 properties of PBF-E-processed Ni-based SX superalloys, Meid et al. [6] compared the LCF life at 950 °C at a

346 stress ratio 0.6 of the AM SX with its parent cast material fully heat treated with and without HIP. They showed
347 that the former performed better than the latter. In contrast, they did not report any failure related to the presence
348 of grain boundaries probably because these stray grains were avoided by machining the samples from the center
349 of bars. According to Meid's results [6] the crack initiation for PBF-E SX has three potential sources: (i) the
350 interface of melting layers, (ii) the micro-porosity generated during solidification or, (iii) for the HIPed specimens,
351 the precipitates formed at the location of collapsed pores. However, none of their specimens initiated or failed
352 from the surface and we have to recall that the fatigue conditions used by Meid et al. introduced a pronounced
353 cyclic ratcheting, i.e. creep strongly contributed to the damage mechanisms [6].

354 The following discussion will hence focus on the VHCF damage mechanisms of PBF-E-processed specimens,
355 with a special focus on the crack initiation mechanism from the surface assisted by oxidation.

356

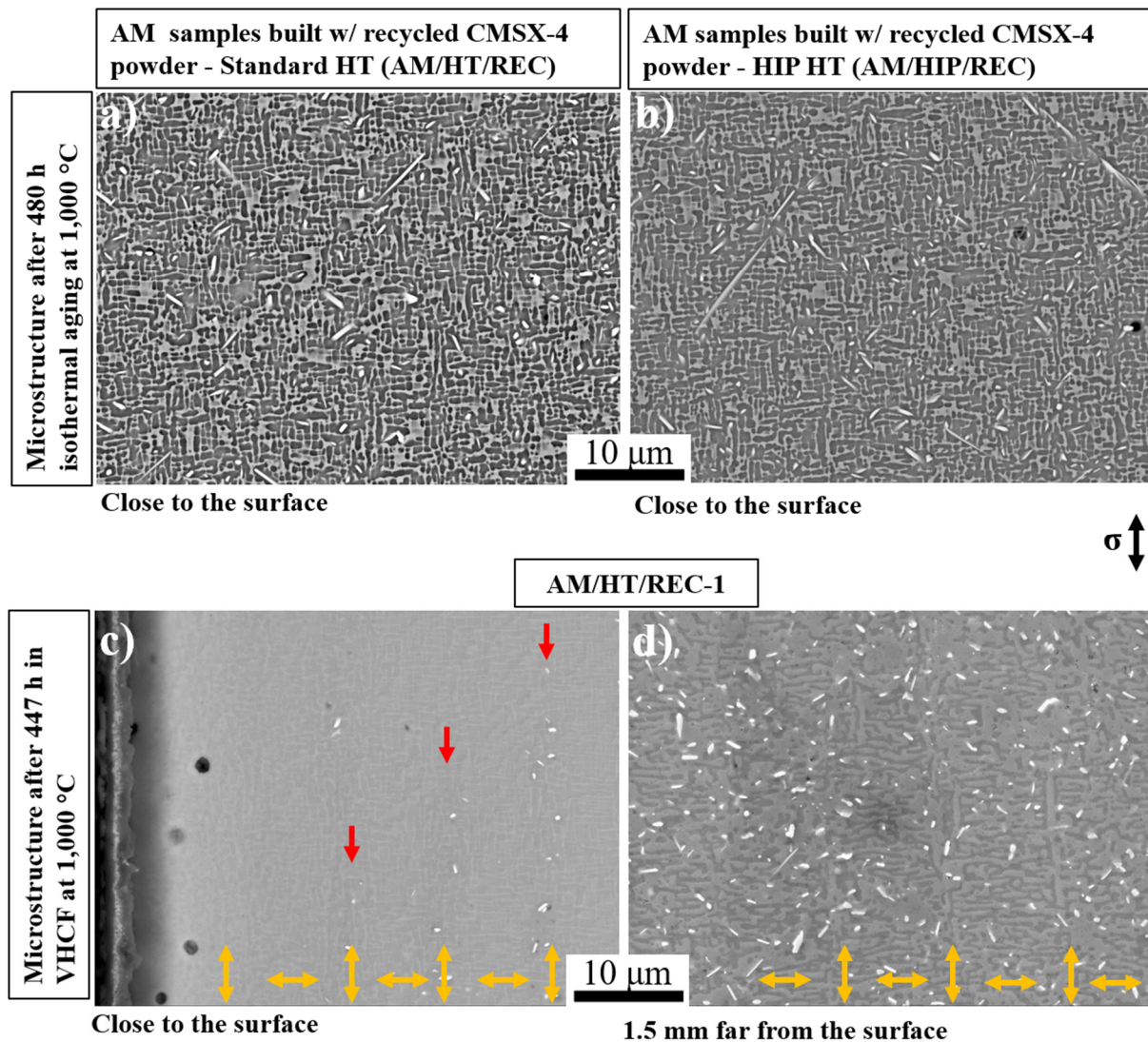
357 *4.1. Crack initiation at grain boundaries*

358 According to **Fig. 3** and **Table 3**, the presence of stray grains within the gauge part of VHCF specimens induces
359 a spectacular debit in fatigue life. Six specimens even failed during the initial ramping-up in alternating stress (see
360 **Fig. 4**). These grains are either inherited from the PBF-E building process (i.e., the polycrystalline shell as shown
361 in **Fig. 1a** could have been deeper in some AM processed specimens leading to the presence of grains within the
362 gauge part of specimens after machining/polishing) and/or the HIPing process. While (surface) recrystallization is
363 known to decrease the LCF life of Ni-based single crystalline superalloys [34,35], no prior study reported on the
364 consequence of stray grain on the VHCF life at high temperature of Ni-based SX superalloys, according to the
365 authors' best knowledge. We may only mention that a directionally solidified alloy (DS200+Hf), presenting
366 several $\approx \langle 001 \rangle$ columnar grains within the gauge part of VHCF specimens (i.e. low angle grain boundaries with
367 respect to the loading direction [36]), performs slightly worse in VHCF at 1,000 °C/ $R_\epsilon = -1/f = 20$ kHz compared
368 to SX specimens solidified with the same casting parameters [15]. Hence, highly misoriented grains from the
369 perfect [001] crystallographic orientation is critical to the VHCF life. In fact, as VHCF specimens used in the
370 present study are designed so as to obtain a frequency of resonance in tension/compression of 20 kHz \pm 500 Hz
371 [32], such recrystallized grains have a Young's modulus far higher than the one along the $\langle 001 \rangle$ orientation (i.e.
372 93 GPa for CMSX-4/Bridgman). Hence, the local frequency of resonance is far different from 20 kHz leading to
373 a local stress concentration at grain boundaries. Failure in shear mode at the grain boundary is obtained in such a
374 condition. The analysis of the role of recrystallized grains on the VHCF life of Ni-based SX superalloy specimens
375 will be analyzed in greater details in a forthcoming article, by using finite element simulations and bicrystalline
376 specimens tested in VHCF in the same condition.

377

378 *4.2. Microstructure evolution*

379 PBF-E specimens that failed through cracks whose nucleation/micropropagation is assisted by oxidation presented
380 a very high VHCF life (between 70 and 447 h) at 1,000 °C. According to **Figs. 11** and **12**, these specimens
381 presented very different intermetallic precipitates in addition to the usual γ precipitates. AM/HT/REC and
382 AM/HIP/REC coupons were then overaged in isothermal conditions for 480 h at 1,000 °C to compare the
383 microstructure evolutions with and without ultrasonic fatigue loading. Such a comparison is shown in **Fig.13**.



384

385 **Fig. 13.** (a) Microstructure evolution after 480 h at 1,000 °C for AM/HT/REC and (b) AM/HIP/REC. Both
 386 microstructures were taken 0.5 mm below the fracture surface. (c) Microstructure evolution after \approx 447 h in VHCF
 387 at 1,000 °C for AM/HT/REC-1 ($\sigma_a = 145$ MPa, $N_f = 3.2 \times 10^{10}$ cycles) close to the surface and (d) 1.5 mm below
 388 the surface. Red arrows are showing TCP precipitates along the dendritic zones. Yellow arrows are showing the
 389 directions of local γ coarsening. (For interpretation of the references to color in this figure legend, the reader is
 390 referred to the web version of this article.)

391

392 At 1,000 °C, the superalloy CMSX-4/Bridgman is known to be prone to topologically close-packed (TCP)
 393 precipitates [14,37–40] that are well known to lower the mechanical properties [41,42]. This TCP precipitation is
 394 also known to be enhanced at high temperature by the introduction of pre-deformation [43,44] or by the very high
 395 local plastic deformation in the rough zone close to stress raisers in VHCF [20]. As already investigated by Pistor
 396 et al. [30], TCP phases precipitate in PBF-E CMSX-4 alloy at high temperatures (around 1,050°C) and for longtime
 397 exposures. In our study, based on the morphology and EDS analysis showing a very high Re content shown in **Fig.**
 398 **12**, we believe that needle-type precipitates are also TCP phases [39]. Moreover, AM/HT/REC-1 test lasted \approx 447

399 h, i.e. long enough to be in the precipitation domain of TCP phases at high temperatures according to previous
400 literature [33,38,39], as opposed to the tests performed by Meid et al. [9] that only lasted 48 h in LCF.

401 Such TCP phases precipitate homogeneously ($\approx 1\%$ in area fraction) in the material without loading (**Figs. 13a**
402 **and b**). Comparing **Fig. 13d** (2.5 % in area fraction) with **Figs. 13a and b**, imposing the VHCF loading does not
403 seem to deeply affect the overall amount of TCP phases, but their location varies close to the surface, where they
404 seem to mainly precipitate in former primary dendrite arms (red arrows at **Fig. 13c**). Further, their density increases
405 from the surface towards the bulk. This can be explained by the local change in chemical composition due to the
406 depletion of the other alloying elements to form the oxides, especially Cr and W known to favor TCP precipitation
407 in CMSX-4/Bridgman [33], in addition to Re. This result is also in good agreement with the Re distribution map
408 of **Fig. 12b** showing almost no TCP precipitates close to the crack tip.

409 The square-type precipitates rich in N are the nitrides developed close to the surface due to the low oxygen
410 pressure. As the oxygen is being consumed by the Ni, Al, and Cr elements to form the oxide layer, the oxygen
411 pressure locally drops, and the 78 % of N_2 present in the air diffuses in the substrate reacting with Al and Ti.
412 Nitrides are known to be brittle structures, decreasing the mechanical properties of superalloys, especially in
413 fatigue at low temperatures [45–47]. The Ta/W/Hf-rich carbides previously observed in MAR-M247 [48] and in
414 Mar-M200+Hf/DS200+Hf [49] are also known to favor crack initiation in LCF [50]

415 The voids appearing just beneath the oxide layer (**Figs. 11 b-e**) have been previously observed after the high
416 temperature oxidation of various Ni-based superalloys [51–54] and are related to the vacancy supersaturation
417 according to Evans et al. [55]. Such vacancies originate by the major outward cation diffusion and the
418 countercurrent injection of vacancies into the bulk resulting in the well-known Kirkendall porosity [56]. One shall
419 notice that the Kirkendall porosity often driven by the gradient of chemical potential [57] (**Fig. 12c**) was not
420 observed in the absence of mechanical loading. This finding suggests that greater outward diffusion was most
421 likely enhanced through the dislocations introduced upon the VHCF [58] allowing to reach voids of $\approx 5\ \mu\text{m}$
422 diameter. One may also speculate on the high dislocations' density inherited from the very PBF-E additive
423 manufacturing process that can also foster oxidation. Indeed, it is known that a very high dislocation density is
424 present within the material after the PBF-E process [59], and this was also confirmed by the fact it has been
425 impossible to conduct VHCF tests in the present conditions at alternating stresses greater than 180 MPa (see Fig.
426 2), due to a too pronounced self-heating. Regarding oxidation, Juillet et al. demonstrated that the instantaneous
427 parabolic rate (k_p) constants could not be calculated in an AM IN-718 superalloy due to enhanced growth of the
428 oxides in comparison with the forged counterparts and related this to the significantly higher density of internal
429 defects assessed by transmission electron microscopy (TEM) [60]. As a result, the selective outward diffusion of
430 the most oxidizable elements to form the oxide scale brings about the precipitation of the strong carbide and nitride
431 formers underneath [61].

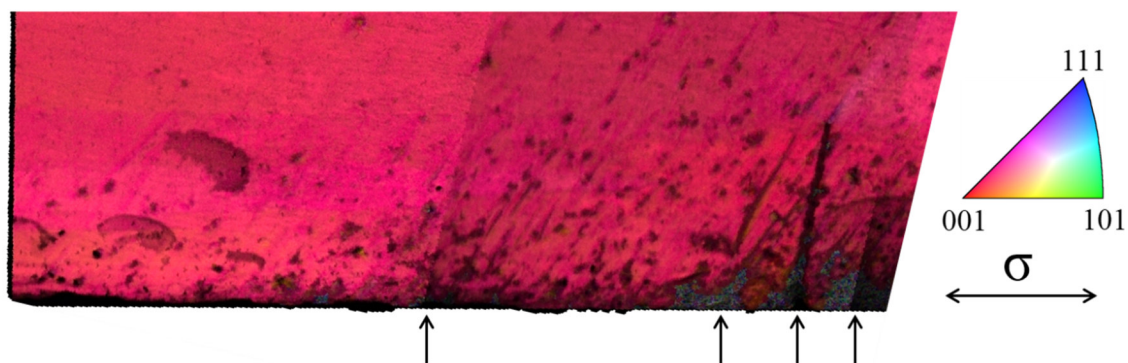
432

433 *4.3. Crack initiation and propagation mechanism assisted by oxidation*

434 This is the first time that a VHCF life controlled by oxidation is presented in the open literature for a Ni-based SX
435 superalloy at high temperature in fully reversed conditions, and in the absence of any surface recrystallization
436 mechanisms. In fact, several EBSD maps have been performed in this work for specimens showing surface crack

437 initiation and no evidence of recrystallization close to secondary cracks in PBF-E processed specimens has been
 438 observed (see, e.g., Fig. 14). Cervellon already observed that surface cracks may develop in fully reversed
 439 conditions at the same temperature for long VHCF tests [15,17], but the main crack initiation (almost) always
 440 occurred at an internal site (a casting pore). Our present results are somehow different from previous examples of
 441 fatal crack initiation from the surface in VHCF in this class of alloys showing the presence of recrystallized grains
 442 (associated or not to a coating deposition process) [21,22] or from a stress concentration at the surface of
 443 specimens, due to a prior plastic deformation before testing specimens in VHCF at $1,000^{\circ}\text{C}/R=0.5/f = 20 \text{ kHz}$
 444 [23].

445

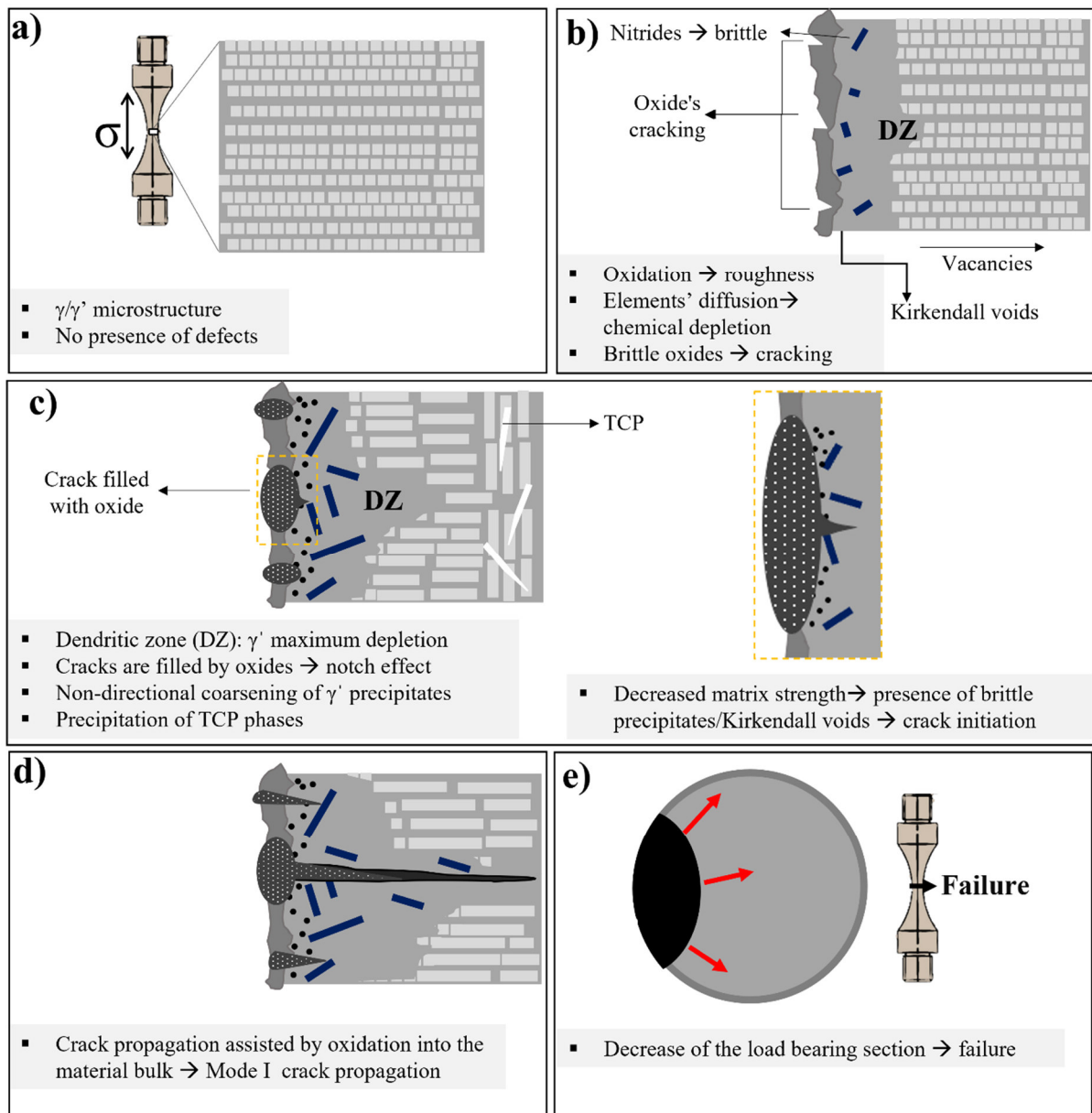


446

447 **Fig. 14.** EBSD characterization of AM/HT/REC-1 ($\sigma_a = 145 \text{ MPa}$, $N_f = 3.2 \times 10^{10}$ cycles) close to surface
 448 secondary cracks. The Index Quality map is superimposed to the inverse pole figure (IPF) relative to the loading
 449 direction. Black arrows indicate secondary cracks initiated from the surface.

450

451 **Fig. 15** presents the typical crack initiation mechanism as understood from the microstructures and chemical
 452 analyses shown before. Starting from the initial optimized γ/γ' microstructure (**Fig. 15a**) that likely contains
 453 intrinsic processing defects (incl. a high dislocation density), oxidation rapidly occurs at the specimens' surface,
 454 leading to a rougher surface and to the depletion of (mostly) Al and Cr and the subsequent precipitation of nitrides
 455 and carbides below the surface (**Fig. 15b**). Dislocation climbing may be then fostered with the VHCF loading,
 456 results in enhanced outward cation diffusion and the derived formation of Kirkendall voids just below the free
 457 surface (**Fig. 15c**). Increasing the duration of VHCF exposure at high temperature leads to TCP precipitation and
 458 to non-directional coarsening of γ' precipitates (see **Fig. 15c**), resulting from a small remaining dendritic
 459 segregation, as already proposed by Hazotte et al. [62]. Overall, the subsurface layer is composed of voids, a γ
 460 matrix depleted from its main refractory elements filled with quite brittle particles (nitrides, carbides). The
 461 increased surface roughness due to oxidation combined with the presence these voids/non-metallic inclusions lead
 462 to a surface crack initiation at a void or a non-metallic particle. This micro-crack then propagates in mode I through
 463 the microstructure, assisted by oxidation, up to failure (**Figs. 15d** and **e**).



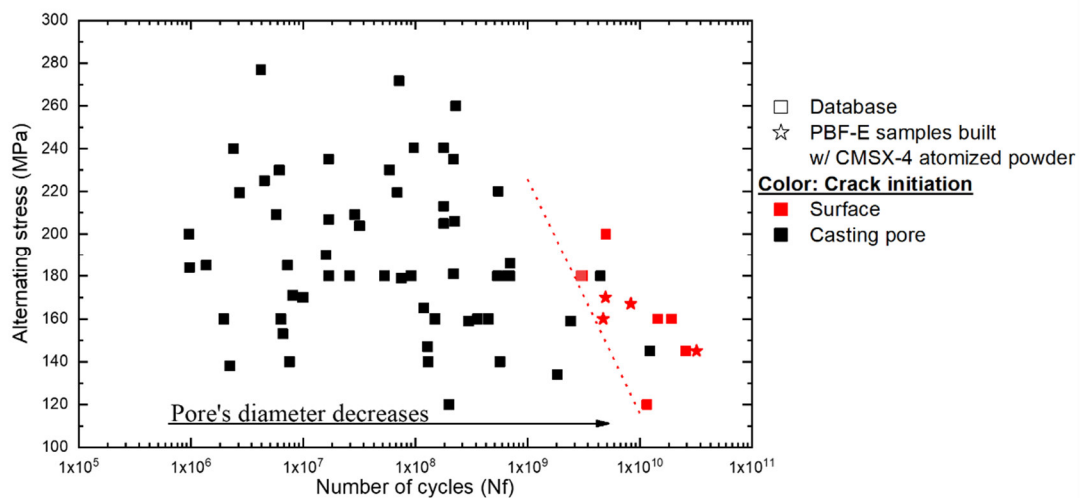
464

465 **Fig. 15.** Schematic illustration of the oxidation-controlled crack initiation mechanism of PBF-E CMSX-4 SX Ni-
 466 based superalloys in VHCF conditions at 1,000 °C/ $R_\epsilon = -1/f = 20$ kHz. (a) The initial optimized γ/γ' microstructure
 467 is oxidized leading to the precipitation of nitrides (b) and carbides below the surface and simultaneously
 468 developing a rougher surface. (c) Subsequently the oxidation leads to the formation of Kirkendall voids just below
 469 the free surface, followed by the precipitation of TCP phases as well as non-directional coarsening of γ' precipitates.
 470 The increased surface roughness due to oxidation combined with the presence these voids/non-metallic inclusions
 471 lead to a surface crack initiation at a void or a non-metallic particle. (d) The micro-crack then propagates in mode
 472 I through the microstructure, assisted by oxidation, up to failure (e). (For interpretation of the references to color
 473 in this figure legend, the reader is referred to the web version of this article.)

474

475 From the present investigation, it has been shown that provided PBF-E processed CMSX-4 specimens are defect-
 476 free (i.e., no stray grain within the gauge part of specimens), a very high VHCF life is obtained, comparable or

477 even longer than the one obtained for conventionally processed Ni-based SX superalloys. A S-N diagram at 1,000
 478 °C/ $R_e = -1/f = 20$ kHz including defect-free PBF-E processed CMSX-4 specimens and several other results
 479 obtained for conventionally processed Ni-based SX superalloys with an internal crack initiation at a solidification
 480 pore is shown in the **Fig. 16**. It is important to point out that the results from the internal database in Institut
 481 Pprime/ISAE-ENSMA (France) have been obtained using “legacy” Ni-based SX superalloys such as Rene N5 and
 482 AM1 [63] and but also newer generations such as CMSX-4 Plus, DD33, TMS-238, MC-NG, and TROPEA
 483 [18,19,63]. Their chemical composition is given in **Table 4**. Further, they were solidified using a Bridgman or an
 484 LMC process. According to **Fig. 16**, an environmental VHCF limit under such conditions can clearly be identified,
 485 towards the highest VHCF lives. Up to now, most of the authors focused their investigations on VHCF damage
 486 mechanisms from either casting pores or from non-metallic inclusions (TCP phases, eutectics, carbides...), i.e.
 487 from process related “defects” [15,19,20,57,64]. When nearly all such defects are removed from the material, and
 488 provided that a good surface preparation of specimens is performed to avoid any surface recrystallization due to
 489 too large residual stresses known to be detrimental the fatigue life [34,35], the intrinsic VHCF life is controlled by
 490 the alloy’s chemistry. In such conditions, the VHCF life of single crystalline Ni-based superalloys is hence
 491 controlled by the environmental resistance of the alloy, i.e., by its own chemistry and the overall microstructure
 492 of the alloys. The present study also suggests that no fatigue limit exists in these fatigue conditions at high
 493 temperature, but such a question should also be investigated at higher and lower temperatures to get a better picture
 494 of oxidation controlled VHCF crack initiation mechanisms.



495
 496 **Fig. 16.** S-N diagram at 1,000 °C, $R_e = -1 / f = 20$ kHz including defect-free PBF-E processed CMSX-4 SX
 497 specimens and other “conventionally” processed SX specimens made of Rene N5, AM1, CMSX-4 Plus, DD33,
 498 TMS-238, MC-NG and TROPEA alloys with different solidification parameters [18,19,63]. The alternating stress
 499 σ_a is plotted as a function of the number of cycles to failure. A transition from an internal crack initiation site at a
 500 large casting pore to the surface is illustrated. (For interpretation of the references to color in this figure legend,
 501 the reader is referred to the web version of this article.)

502

503 **Table 4**

504 Chemical composition (in wt. pct) of AM1, Rene N5, CMSX-4 Plus, DD33, TMS-238, MC-NG and
505 TROPEA alloys

Alloy	Ni	Cr	Mo	Co	W	Al	Ti	Ta	Hf	Re	Others
AM1	Bal.	7.5	2.0	6.6	5.5	5.2	1.2	7.9	0.1		
Rene N5	Bal.	7.0	2.0	8.0	5.0	6.2		7.0	0.2	3.0	
CMSX-4 Plus	Bal.	3.5	0.6	10.0	6.0	5.7	0.9	8.0	0.1	4.8	
DD33 [65]	Bal.	3.0	1.0	12.0	6.0	6.0		8.0	0.1	4.0	
TMS-238 [66]	Bal.	4.6	1.1	6.5	4.0	5.9		7.6	0.1	6.4	5.0 Ru
MCNG [67]	Bal.	4.0	1.0	<0.2	5.0	6.0	0.5	5.0	0.1	4.0	4.0 Ru
TROPEA [68]	Bal.	6.4	0.6	8.9	6.1	5.4	1.0	9.1	0.08	1.0	1.95 Pt

506

507 **5. Conclusions**

508 Very high cycle fatigue performances and crack initiation mechanisms at high temperature of PBF-E CMSX-4 SX
509 Ni-based superalloy have been investigated under fully reversed conditions ($R_\epsilon = -1$), $f = 20$ kHz and $1,000$ °C.
510 Comparisons have been made with conventionally processed Ni-based SX superalloys of ERBO/1 and CMSX-
511 4/Bridgman type. The following main conclusions have been obtained:

- 512 • All Bridgman processed specimens failed from an internal casting pore site.
- 513 • The VHCF lifetime of PBF-E processed specimens in these conditions is comparable or higher than the
514 one of Bridgman solidified Ni-based SX superalloys provided that no defect (e.g., stray grain) is present
515 within the gauge part of the specimens.
- 516 • The presence of high angle grain boundaries/stray grains leads to a spectacular (more than 3 decades)
517 decrease in VHCF lifetime compared to defect-free specimens.
- 518 • Due to the absence of large casting pores/non-metallic inclusions, nearly all defect-free PBF-E processed
519 specimens failed by an oxidation assisted surface crack initiation process. Hence, the superalloy chemistry
520 and microstructure stability below the surface controls the crack initiation and first stages of propagation
521 and an environmentally controlled VHCF life limit has been identified in these conditions.

522

523

524

525 **Acknowledgements**

526 The authors wish to thank Florence Hamon, Florent Mauget and Jacques Lefort (Physics and Mechanics of
527 Materials Department, Institut Pprime, France) for their help and advice during mechanical testing and
528 microstructural observations. Institut Pprime gratefully acknowledges “Contrat de Plan Etat - Région Nouvelle-
529 Aquitaine (CPER)” as well as the “Fonds Européen de Développement Régional (FEDER)” for their financial
530 support to the reported work. Part of this study was supported by the Nouvelle-Aquitaine French region through
531 the ECOREVE project (project number 2018-1R10122). This study is also part of the "Self-Heating" ANR-Safran-
532 Naval group research chair (Grant # ANR-20-CHIN-0002) involving the Safran Companies, Naval group, ENSTA
533 Bretagne (IRDL) and Institut Pprime. F. Pedraza gratefully acknowledges the CNRS for funding his secondment
534 period at Institut Pprime. Institute of Metal Research, Shenyang, P.R. China (Pr. J. Zhang) and Safran Aircraft
535 Engines are acknowledged for providing DD33 and AM1/Rene N5 materials used in the final discussion,
536 respectively. The authors acknowledge funding by the Deutsche Forschungsgemeinschaft (DFG) in the framework
537 of the collaborative research center SFB/TR 103 through projects B2 (JP, CK) and T4 (ILG, BR, WT).

538

539 **References**

- 540 [1] R.C. Reed, *The superalloys - Fundamentals and applications*, First edit, Cambridge University Press,
541 Cambridge, 2006.
- 542 [2] T.M. Pollock, S. Tin, *Nickel-Based Superalloys for Advanced Turbine Engines: Chemistry,*
543 *Microstructure and Properties*, *J. Propuls. Power.* 22 (2008) 361–374.
- 544 [3] P. Caron, T. Khan, *Evolution of Ni-based superalloys for single crystal gas turbine blade applications,*
545 *Aerosp. Sci. Technol.* 3 (1999) 513–523.
- 546 [4] M. Perrut, P. Caron, M. Thomas, A. Couret, *High temperature materials for aerospace applications: Ni-*
547 *based superalloys and γ -TiAl alloys*, *Comptes Rendus Phys.* 19 (2018) 657–671.
- 548 [5] E. Chauvet, C. Tassin, J.J. Blandin, R. Dendievel, G. Martin, *Producing Ni-base superalloys single crystal*
549 *by selective electron beam melting*, *Scr. Mater.* 152 (2018) 15–19.
- 550 [6] C. Körner, M. Ramsperger, C. Meid, D. Bürger, P. Wollgramm, M. Bartsch, G. Eggeler, *Microstructure*
551 *and Mechanical Properties of CMSX-4 Single Crystals Prepared by Additive Manufacturing*, *Metall.*
552 *Mater. Trans. A Phys. Metall. Mater. Sci.* 49 (2018) 3781–3792.
- 553 [7] K. Harris, G.L. Erickson, S.L. Sikkenga, W.D. Brentnall, J.M. Aurrecochea, K.G. Kubarych,
554 *Development of two rhenium- containing superalloys for single- crystal blade and directionally solidified*
555 *vane applications in advanced turbine engines*, in: *Superalloys 1992*, 1992: pp. 297–306.
- 556 [8] K. Harris, J.B. Wahl, *Improved single crystal superalloys, CMSX-4@(SLS)[La+Y] and CMSX-486@,*
557 *Proc. Int. Symp. Superalloys.* (2004) 45–52.
- 558 [9] C. Meid, A. Dennstedt, M. Ramsperger, J. Pistor, B. Rutttert, I. Lopez-Galilea, W. Theisen, C. Körner, M.
559 Bartsch, *Effect of heat treatment on the high temperature fatigue life of single crystalline nickel base*
560 *superalloy additively manufactured by means of selective electron beam melting*, *Scr. Mater.* 168 (2019)

- 561 124–128.
- 562 [10] P. Caron, T. Khan, Improvement of creep strength in a nickel-based single-crystal superalloy by heat
563 treatment, *Mater. Sci. Eng.* 61 (1983) 173–184.
- 564 [11] B.C. Wilson, J.A. Hickman, G.E. Fuchs, The effect of solution heat treatment on a single-crystal Ni-based
565 superalloy, *JOM - Res. Summ.* 55 (2003) 35–40.
- 566 [12] Transregio, (n.d.). <https://www.sfb-transregio103.de>.
- 567 [13] W.J. Zhang, Thermal mechanical fatigue of single crystal superalloys: Achievements and challenges,
568 *Mater. Sci. Eng. A.* 650 (2016) 389–395.
- 569 [14] J.Z. Yi, C.J. Torbet, Q. Feng, T.M. Pollock, J.W. Jones, Ultrasonic fatigue of a single crystal Ni-base
570 superalloy at 1000 °C, *Mater. Sci. Eng. A.* 443 (2007) 142–149.
- 571 [15] A. Cervellon, J. Cormier, F. Mauget, Z. Hervier, Y. Nadot, Very high cycle fatigue of Ni-based single
572 crystal superalloys at high temperature, *Metall. Mater. Trans. A.* 49 (2018) 3938–3950.
- 573 [16] A. Cervellon, J.Z. Yi, F. Corpace, Z. Hervier, J. Rigney, P.K. Wright, C.J. Torbet, J. Cormier, J.W. Jones,
574 T.M. Pollock, Creep, fatigue, and oxidation interactions during High and very high cycle fatigue at
575 elevated temperature of nickel-base single crystal superalloys, in: S. Tin, M. Hardy, J. Clews, J. Cormier,
576 Q. Feng, J. Marcin, C. O'brien, A. Suzuki (Eds.), *Proc. Int. Symp. Superalloys 2020*, Springer US, Seven
577 Springs, PA, USA, 2020: pp. 185–195.
- 578 [17] A. Cervellon, J. Cormier, F. Mauget, Z. Hervier, VHCF life evolution after microstructure degradation of
579 a Ni-based single crystal superalloy, *Int. J. Fatigue.* 104 (2017) 251–262.
- 580 [18] L.M. Bortoluci, S. Utada, J. Rame, L. Mataveli Suave, K. Kawagishi, H. Harada, P. Villechaise, J.
581 Cormier, Tensile, Low Cycle Fatigue, and Very High Cycle Fatigue characterizations of advanced single
582 crystal Nickel-based superalloys, in: S. Tin, M. Hardy, J. Clews, J. Cormier, Q. Feng, J. Marcin, C.
583 O'brien, A. Suzuki (Eds.), *Proc. Int. Symp. Superalloys 2020*, Springer US, Seven Springs, PA, USA,
584 2020: pp. 341–351.
- 585 [19] L.M. Bortoluci, L. Mataveli Suave, A. Cervellon, P. Villechaise, J. Cormier, LCF, HCF and VHCF life
586 sensitivity to solution heat treatment of a third-generation Ni-based single crystal superalloy, *Int. J.*
587 *Fatigue.* 130 (2020) 105247.
- 588 [20] A. Cervellon, S. Hemery, P. Kürnsteiner, B. Gault, P. Kontis, J. Cormier, Crack initiation mechanism
589 during very high cycle fatigue of Ni-based single crystal superalloys at high temperature, *Acta Mater.* 188
590 (2020) 131–144.
- 591 [21] A. Cervellon, L.M. Bortoluci Ormastroni, Z. Hervier, T.M. Pollock, F. Pedraza, J. Cormier, Damage
592 mechanisms during very high cycle fatigue of a coated and grit-blasted Ni-based single-crystal superalloy,
593 *Int. J. Fatigue.* 142 (2021) 105962.
- 594 [22] Z. Zhao, Q. Li, F. Zhang, W. Xu, B. Chen, Transition from internal to surface crack initiation of a single-
595 crystal superalloys in the very-high-cycle fatigue regime at 1100 °C, *Int. J. Fatigue.* 150 (2021) 106343.
- 596 [23] S. Utada, L.M. Bortoluci, J. Rame, P. Villechaise, J. Cormier, VHCF life of AM1 Ni-based single crystal

- 597 superalloy after pre-deformation, *Int. J. Fatigue*. 148 (2021) 106224.
- 598 [24] I. Lopez-Galilea, B. Rutttert, J. He, T. Hammerschmidt, R. Drautz, B. Gault, W. Theisen, Additive
599 manufacturing of CMSX-4 Ni-base superalloy by selective laser melting: Influence of processing
600 parameters and heat treatment, *Addit. Manuf.* 30 (2019) 100874.
- 601 [25] B. Rutttert, M. Ramsperger, L. Mujica Roncery, I. Lopez-Galilea, C. Körner, W. Theisen, Impact of hot
602 isostatic pressing on microstructures of CMSX-4 Ni-base superalloy fabricated by selective electron beam
603 melting, *Mater. Des.* 110 (2016) 720–727.
- 604 [26] L. Mujica Roncery, I. Lopez-Galilea, B. Rutttert, S. Huth, W. Theisen, Influence of temperature, pressure,
605 and cooling rate during hot isostatic pressing on the microstructure of an SX Ni-base superalloy, *Mater.*
606 *Des.* 97 (2016) 544–552.
- 607 [27] A.B. Parsa, P. Wollgramm, H. Buck, C. Somsen, A. Kostka, I. Povstugar, P.P. Choi, D. Raabe, A. Dlouhy,
608 J. Müller, E. Spiecker, K. Demtroder, J. Schreuer, K. Neuking, G. Eggeler, Advanced scale bridging
609 microstructure analysis of single crystal Ni-base superalloys, *Adv. Eng. Mater.* 17 (2015) 216–230.
- 610 [28] E. Plancher, P. Gravier, E. Chauvet, J.J. Blandin, E. Boller, G. Martin, L. Salvo, P. Lhuissier, Tracking
611 pores during solidification of a Ni-based superalloy using 4D synchrotron microtomography, *Acta Mater.*
612 181 (2019) 1–9.
- 613 [29] M. Ramsperger, L. Mújica Roncery, I. Lopez-Galilea, R.F. Singer, W. Theisen, C. Körner, Solution Heat
614 Treatment of the Single Crystal Nickel-Base Superalloy CMSX-4 Fabricated by Selective Electron Beam
615 Melting, *Adv. Eng. Mater.* 17 (2015) 1486–1493.
- 616 [30] J. Pistor, C. Körner, Formation of topologically closed packed phases within CMSX-4 single crystals
617 produced by additive manufacturing, *Mater. Lett. X.* 1 (2019) 1–4.
- 618 [31] M. Ramsperger, R.F. Singer, C. Körner, Microstructure of the Nickel-Base Superalloy CMSX-4
619 Fabricated by Selective Electron Beam Melting, *Metall. Mater. Trans. A Phys. Metall. Mater. Sci.* 47
620 (2016) 1469–1480.
- 621 [32] A. Cervellon, Propriétés en fatigue à grand et très grand nombre de cycles et à haute température des
622 superalliages base nickel monogranulaires, PhD Thesis - Ecole Nationale Supérieure de Mécanique et
623 d’Aérotechnique (ISAE-ENSMA), France, 2018. <https://tel.archives-ouvertes.fr/tel-01940424/document>.
- 624 [33] B. Dubiel, P. Indyka, I. Kalembe-Rec, A. Kruk, T. Moskalewicz, A. Radziszewska, S. Kaç, A. Kopia, K.
625 Berent, M. Gajewska, The influence of high temperature annealing and creep on the microstructure and
626 chemical element distribution in the γ , γ' and TCP phases in single crystal Ni-base superalloy, *J. Alloys*
627 *Compd.* 731 (2018) 693–703.
- 628 [34] X. Ma, H.J. Shi, J. Gu, Z. Yang, G. Chen, O. Luesebrink, H. Harders, Influence of surface recrystallization
629 on the low cycle fatigue behaviour of a single crystal superalloy, *Fatigue Fract. Eng. Mater. Struct.* 38
630 (2015) 340–351.
- 631 [35] X. Ma, J. Jiang, W. Zhang, H.J. Shi, J. Gu, Effect of local recrystallized grains on the low cycle fatigue
632 behavior of a nickel-based single crystal superalloy, *Crystals.* 9 (2019) 312.

- 633 [36] L. Mataveli Suave, J. Cormier, P. Villechaise, D. Bertheau, G. Benoit, F. Mauget, G. Cailletaud, L. Marcin,
634 High Temperature Creep Damage Mechanisms in a Directionally Solidified Alloy: Impact of
635 Crystallography and Environment, in: M.C. Hardy, E. Huron, U. Glatzel, B. Griffin, B. Lewis, C.M.F.
636 Rae, V. Seetharaman, S. Tin (Eds.), Proc. Int. Symp. Superalloys, TMS (The Minerals, Metals & Materials
637 Society), Seven Springs, 2016: pp. 747–756.
- 638 [37] R. Giraud, Influence de l’histoire thermique sur les propriétés mécaniques à haute et très haute température
639 du superalliage monocristallin CMSX-4®, PhD Thesis - Ecole Nationale Supérieure de Mécanique et
640 d’Aérotechnique (ISAE-ENSMA), France, 2014. <https://www.theses.fr/2014ESMA0005>.
- 641 [38] K. Cheng, C. Jo, T. Jin, Z. Hu, Precipitation behavior of μ phase and creep rupture in single crystal
642 superalloy CMSX-4, *J. Alloys Compd.* 509 (2011) 7078–7086.
- 643 [39] C.M.F. Rae, R.C. Reed, The precipitation of topologically close-packed phases in rhenium-containing
644 superalloys, *Acta Mater.* 49 (2001) 4113–4125.
- 645 [40] I. Lopez-Galilea, J. Kofmann, A. Kostka, R. Drautz, L. Mujica Roncery, T. Hammerschmidt, S. Huth, W.
646 Theisen, The thermal stability of topologically close-packed phases in the single-crystal Ni-base superalloy
647 ERBO/1, *J. Mater. Sci.* 51 (2016) 2653–2664.
- 648 [41] J.B. le Graverend, J. Cormier, S. Kruch, F. Gallerneau, J. Mendez, Microstructural parameters controlling
649 high-temperature creep life of the nickel-base single-crystal superalloy MC2, *Metall. Mater. Trans. A*
650 *Phys. Metall. Mater. Sci.* 43 (2012) 3988–3997.
- 651 [42] M. Simonetti, P. Caron, Role and behaviour of μ phase during deformation of a nickel-based single crystal
652 superalloy, *Mater. Sci. Eng. A.* 254 (1998) 1–12.
- 653 [43] C. Meid, M. Eggeler, P. Watermeyer, A. Kostka, T. Hammerschmidt, R. Drautz, G. Eggeler, M. Bartsch,
654 Stress-induced formation of TCP phases during high temperature low cycle fatigue loading of the single-
655 crystal Ni-base superalloy ERBO/1, *Acta Mater.* 168 (2019) 343–352.
- 656 [44] B.G. Choi, C.Y. Jo, H.U. Hong, I.S. Kim, S.M. Seo, H.M. Kim, Effect of pre-strain on microstructural
657 evolution during thermal exposure of single crystal superalloy CMSX-4, *Trans. Nonferrous Met. Soc.*
658 *China (English Ed.)* 21 (2011) 1291–1296.
- 659 [45] A. Govaere, A.-L. Rouffie, J.M. Franchet, D. Galy, C. Dumont, A. Devaux, C. Crozet, P. Kontis, P.
660 Villechaise, J. Cormier, Is the Carbon Content Really an Issue for the LCF Durability of Forged γ/γ' Ni-
661 Based Disk Alloys?, in: S. Tin, M. Hardy, J. Clews, J. Cormier, Q. Feng, J. Marcin, C. O’Brien, A. Suzuki
662 (Eds.), Proc. Int. Symp. Superalloys 2020, Springer US, Seven Springs, PA, USA, 2020: pp. 591–602.
- 663 [46] D. Texier, A. Casanova-Gómez, S. Pierret, J.M. Franchet, T.M. Pollock, P. Villechaise, J. Cormier,
664 Microstructural Features Controlling the Variability in Low-Cycle Fatigue Properties of Alloy Inconel
665 718DA at Intermediate Temperature, *Metall. Mater. Trans. A Phys. Metall. Mater. Sci.* 47 (2016) 1096–
666 1109.
- 667 [47] D. Texier, J. Cormier, P. Villechaise, J.C. Stinville, C.J. Torbet, S. Pierret, T.M. Pollock, Crack initiation
668 sensitivity of wrought direct aged alloy 718 in the very high cycle fatigue regime: the role of non-metallic
669 inclusions, *Mater. Sci. Eng. A.* 678 (2016) 122–136.

- 670 [48] A. Szczotok, K. Rodak, Microstructural studies of carbides in MAR-M247 nickel-based superalloy, IOP
671 Conf. Ser. Mater. Sci. Eng. 35 (2012) 012006.
- 672 [49] L. Mataveli Suave, A. Serrano Muñoz, A. Gaubert, G. Benoit, L. Marcin, P. Kontis, P. Villechaise, J.
673 Cormier, Thin-Wall Debit in Creep of DS200 + Hf Alloy, Metall. Mater. Trans. A. 49 (2018) 4021–4028.
- 674 [50] L. Mataveli Suave, High temperature durability of DS200+Hf alloy, PhD Thesis - Ecole Nationale
675 Superieure de Mecanique et d’Aerotechnique (ISAE-ENSMA), France, 2017.
676 <https://www.theses.fr/2017ESMA0032>.
- 677 [51] P. Berthod, Kinetics of High Temperature Oxidation and Chromia Volatilization for a Binary Ni–Cr Alloy,
678 Oxid. Met. 64 (2005) 235–252.
- 679 [52] Y. Shida, G.C. Wood, F.H. Stott, D.P. Whittle, B.D. Bastow, Intergranular oxidation and internal void
680 formation in Ni-40% Cr alloys, Corros. Sci. 21 (1981) 581–597.
- 681 [53] A.H. Rosenstein, J.K. Tien, W.D. Nix, Void Formation in Inconel MA-754 By High Temperature
682 Oxidation., Metall. Trans. A, Phys. Metall. Mater. Sci. 17 A (1986) 151–162.
- 683 [54] J.H. Weber, P.S. Gilman, Environmentally induced porosity in NiCr and NiCr oxide dispersion
684 strengthened alloys, Scr. Metall. 18 (1984) 479–482.
- 685 [55] H.E. Evans, Cavity formation and metallurgical changes induced by growth of oxide scale, Mater. Sci.
686 Technol. (United Kingdom). 4 (1988) 1089–1098.
- 687 [56] E.O. Kirkendall, Diffusion of Zinc in Alpha Brass, Trans. Metall. Soc. AIME. 147 (1942) 104.
- 688 [57] C. Desgranges, F. Lequien, E. Aublant, M. Nastar, D. Monceau, Depletion and voids formation in the
689 substrate during high temperature oxidation of Ni-Cr alloys, Oxid. Met. 79 (2013) 93–105.
- 690 [58] J. Ma, W. Jiang, J. Wang, Y. Zhang, Z. Zhang, Initial oxidation behavior of a single crystal superalloy
691 during stress at 1150 °C, Sci. Rep. 10 (2020) 1–9.
- 692 [59] A.B. Parsa, M. Ramsperger, A. Kostka, C. Somsen, C. Körner, G. Eggeler, Transmission electron
693 microscopy of a CMSX-4 Ni-base superalloy produced by selective electron beam melting, Metals. 6
694 (2016) 258.
- 695 [60] C. Juillet, A. Oudriss, J. Balmain, X. Feaugas, F. Pedraza, Characterization and oxidation resistance of
696 additive manufactured and forged IN718 Ni-based superalloys, Corros. Sci. 142 (2018) 266–276.
- 697 [61] F. Pedraza, R. Troncy, A. Pasquet, J. Delautre, S. Hamadi, Critical Hafnium Content for Extended Lifetime
698 of AM1 Single Crystal Superalloy, in: S. Tin, M.C. Hardy, J. Clews, J. Cormier, Q. Feng, J. Marcin, C.
699 O’Brien, A. Suzuki (Eds.), Proc. Int. Symp. Superalloys 2020, Springer US, Seven Springs, PA, USA,
700 2020: pp. 781–788.
- 701 [62] A. Hazotte, J. Lacaze, Chemically oriented γ' plate development in a nickel base superalloy, Scr. Metall.
702 23 (1989) 1877–1882.
- 703 [63] L.M. Bortoluci Ormastroni, Ni-based single-crystal superalloy fatigue crack initiation shift from internal
704 sites to the surface at high temperatures, PhD Thesis - École Nationale Supérieure de Mécanique et

- 705 d'Aérotechnique (ENSMA), 2022.
- 706 [64] H. Mayer, Fatigue crack growth and threshold measurements at very high frequencies, *Int. Mater. Rev.* 44
707 (1999) 1–34.
- 708 [65] W. Yang, S. Hu, M. Huo, D. Sun, J. Zhang, L. Liu, Orientation controlling of Ni-based single-crystal
709 superalloy by a novel method: Grain selection assisted by un-melted reused seed, *J. Mater. Res. Technol.*
710 8 (2019) 1347–1352.
- 711 [66] K. Kawagishi, A.C. Yeh, T. Yokokawa, T. Kobayashi, Y. Koizumi, H. Harada, Development of an
712 Oxidation-Resistant High-Strength Sixth-Generation Single-Crystal Superalloy TMS-238, in: E.S. Huron,
713 R.C. Reed, M.C. Hardy, M.J. Mills, R.E. Montero, P.D. Portella, J. Telesman (Eds.), *Int. Symp.*
714 *Superalloys*, TMS (The Minerals, Metals & Materials Society), Seven Springs, 2012: pp. 189–195.
- 715 [67] P. Caron, High gamma prime solvus new generation Nickel-based superalloys for single crystal turbine
716 blade applications, in: T.M. Pollock, R.D. Kissinger, R.R. Bowman, K.A. Green, M. McLean, S. Olson,
717 J.J. Schirra (Eds.), *Proc. Int. Symp. Superalloys 2000*, Springer US, Seven Springs, PA, USA, 2000: pp.
718 737–746.
- 719 [68] J. Rame, S. Utada, L.M. Bortoluci Ormastroni, L. Mataveli Suave, L. Despres, P. Kontis, J. Cormier,
720 Platinum containing new generation nickel-based superalloys for single crystalline applications, in: S. Tin,
721 M. Hardy, J. Clews, J. Cormier, Q. Feng, J. Marcin, C. O'brien, A. Suzuki (Eds.), *Proc. Int. Symp.*
722 *Superalloys 2020*, Springer US, Seven Springs, PA, USA, 2020: pp. 71–81.
- 723